Cortactin promotes exosome secretion by controlling branched actin dynamics

Seema Sinha,[1] Daisuke Hoshino,[3] Nan Hyung Hong,[1] Kellye C. Kirkbride,[1] Nathan E. Grega-Larson,[2] Motoharu Seiki,[4] Matthew J. Tyska,[2] and Alissa M. Weaver[1,2,5]

[1]Department of Cancer Biology and [2]Department of Cell and Developmental Biology, Vanderbilt University Medical School, Nashville, TN 37232
[3]Kanagawa Cancer Center, Yokohama 241-0815, Japan
[4]Division of Cancer Cell Research, Institute of Medical Science, The University of Tokyo, Tokyo 108-8639, Japan
[5]Department of Pathology, Microbiology, and Immunology, Vanderbilt University Medical Center, Nashville, TN 37232

Exosomes are extracellular vesicles that influence cellular behavior and enhance cancer aggressiveness by carrying bioactive molecules. The mechanisms that regulate exosome secretion are poorly understood. Here, we show that the actin cytoskeletal regulatory protein cortactin promotes exosome secretion. Knockdown or overexpression of cortactin in cancer cells leads to a respective decrease or increase in exosome secretion, without altering exosome cargo content. Live-cell imaging revealed that cortactin controls both trafficking and plasma membrane docking of multivesicular late endosomes (MVEs). Regulation of exosome secretion by cortactin requires binding to the branched actin nucleating Arp2/3 complex and to actin filaments. Furthermore, cortactin, Rab27a, and coronin 1b coordinately control stability of cortical actin MVE docking sites and exosome secretion. Functionally, the addition of purified exosomes to cortactin-knockdown cells rescued defects of those cells in serum-independent growth and invasion. These data suggest a model in which cortactin promotes exosome secretion by stabilizing cortical actin-rich MVE docking sites.

Introduction

Exosomes are small extracellular vesicles that carry bioactive protein and RNA cargoes and are secreted upon fusion of multivesicular late endosomes (MVEs) with the plasma membrane (PM; Théry, 2011; Raposo and Stoorvogel, 2013). Exosomes control various cellular and organismal functions, including immune cell communication, coagulation, and Drosophila mating behavior (Aharon et al., 2008; Mittelbrunn et al., 2011; Aatonen et al., 2014; Choudhuri et al., 2014; Corrigan et al., 2014). In cancer, exosome secretion can promote tumor growth, angiogenesis, and metastasis and alter the tumor microenvironment (Bobrie et al., 2012; Peinado et al., 2012; Kucharzewska et al., 2013; van Balkom et al., 2013; Costa-Silva et al., 2015; Hoshino et al., 2015).

Recent studies have demonstrated secretion of exosomes by diverse cell types (Théry, 2011; EL Andaloussi et al., 2013) and identified key regulators of MVE docking and fusion with the PM, including Ral1, Rab35, Rab27, and synaptotagmin-7 (Hsu et al., 2010; Ostrowski et al., 2010; Bobrie et al., 2012; Hoshino et al., 2013b; Hyenne et al., 2015). Deregulation of Rab27 and Rab35 in cancer suggests that cancer cells may develop mechanisms to control exosome secretion (Hendrix et al.,

2010; Dong et al., 2012; Ho et al., 2012; Allaire et al., 2013). Exosomes can also be regulated earlier in the endocytic trafficking pathway. Thus, receptor ubiquitination, ceramide synthesis, or recruitment of adaptor molecules can regulate intraluminal vesiculation and cargo content (Trajkovic et al., 2008; Sorkin and von Zastrow, 2009; Baietti et al., 2012; Hyenne et al., 2015). However, the molecular mechanisms that control and promote exosome secretion are still poorly understood.

Cortactin is an actin-binding protein that is overexpressed in many tumors and controls diverse branched actin-dependent processes, including cell motility, invasion, and membrane trafficking (Kirkbride et al., 2011). In head and neck squamous cell carcinoma, cortactin overexpression is associated with decreased patient survival (Schuuring et al., 1992; Schuuring, 1995; Rodrigo et al., 2000, 2009; Yuan et al., 2003). Recently, we identified cortactin as a key regulator of late endosomal trafficking (Sung et al., 2011; Kirkbride et al., 2012; Hong et al., 2015). Cortactin also regulates invadopodia, which are branched actin-rich PM sites of matrix degradation and MVE docking sites (Kirkbride et al., 2011; Hoshino et al., 2013b).

Here, we report that cortactin levels control the number of exosomes secreted from cancer cells. We confirm a role for cortactin in late endosomal trafficking (Kirkbride et al., 2012;

The Rockefeller University Press $30.00
J. Cell Biol. Vol. 214 No. 2   197–213
www.jcb.org/cgi/doi/10.1083/jcb.201601025

JCB   **197**

THE JOURNAL OF CELL BIOLOGY

Hong et al., 2015) and further show that cortactin controls the number of MVE docking sites at the PM. Mechanistically, we find that cortactin, coronin1b, and Rab27a coordinately control actin stability at invadopodial cortical MVE docking sites (Hoshino et al., 2013b) and exosome secretion. Functionally, cortactin-knockdown (KD) cell defects in serum-independent growth and invasion are rescued by addition of purified exosomes. These data indicate that control of branched actin dynamics is a critical regulatory point for exosome secretion.

Results

Cortactin regulates exosome secretion

To test whether cortactin controls exosome secretion, we down-regulated or overexpressed cortactin protein in SCC61 head and neck squamous cell carcinoma cells by expressing specific targeting shRNAs or by overexpression of mouse cortactin (Fig. S1, A and B). To collect exosomes, cells were cultured in Opti-MEM media for 48 h, followed by sequential differential centrifugation of the conditioned media (Thery et al., 2006). Opti-MEM contains growth factors, so it sustains cell growth while avoiding contamination with exosomes from serum. Consistent with our previous finding that cortactin does not affect cell proliferation in a growth factor–replete environment (Clark et al., 2009), cortactin KD did not affect cell number or viability after 48 h in Opti-MEM (Fig. S1, C and D).

To distinguish between microvesicles (MVs; ≥1 μm in size) and exosomes (40–100 nm), the respective 10,000 g and 100,000 g fractions were analyzed by NanoSight nanoparticle tracking analysis (NTA; Fig. S1, E–I; and Fig. 1, A–C). We did not observe differences in the mean number or size of MVs purified from control and cortactin KD cells (Fig. S1, E–I). In contrast, NTA of the exosome fractions revealed a decrease in the number of exosomes secreted by cortactin-KD cells (Fig. 1, A and B). Re-expression of mouse wild-type (WT) cortactin in human-specific cortactin shRNA-expressing cells (see Fig. 5 B) fully rescued exosome secretion (Fig. 1 B, KD1/WT cells). Finally, we found that cortactin overexpression significantly increases exosome secretion (Fig. 1 B, OE). There was no difference in the NTA-calculated mean exosome vesicle size (Fig. 1 C). Analysis of exosome preparations by transmission electron microscopy (TEM; Fig. 1, D–F) confirmed the significant decrease in the number of exosomes secreted from cortactin-KD cells without an effect on vesicle size (Fig. 1, D–F).

To characterize further the exosome fraction, we performed Western blot (WB) analyses. As expected, the vesicles were positive for the exosome markers TSG101, CD63, and Flotillin1 and negative for the Golgi marker GM130 (Fig. 1 G). In addition, the exosomes were positive for several proteins whose trafficking is regulated by cortactin: the matrix metalloproteinases MMP9 and MT1-MMP (Clark et al., 2007, 2009; Clark and Weaver, 2008) and EGFR (Fig. 1 H; Timpson et al., 2005). Because the vesicles were loaded on WB based on equal cell number, KD fractions showed decreased intensity of exosome cargo bands (Fig. 1, G–I). Cortactin-KD or overexpression likewise decreased or increased exosome secretion by HT1080 fibrosarcoma or MDA-MB-231 cells, respectively (Fig. S1, J–O). These data indicate that the level of cortactin expression significantly regulates exosome secretion in cancer cells, both in the positive and negative direction.

Cortactin does not control exosome cargo composition

To determine whether cortactin controls exosome protein cargo composition, shotgun proteomics was performed on an equal number of exosomes purified from SCC61-control and cortactin-KD cells. The results were filtered and collated using IDPicker with a target peptide false discovery rate of 5% and requiring a minimum of two distinct peptides and six spectra per protein identification. This yielded a 4% protein false discovery rate for the nine MudPIT samples (three biological replicates each for control, cortactin-KD1 and KD2 exosomes). Gene Ontology in UniProt database was used to classify the common exosome proteins (Fig. 2 A). Of the 2,102 identified proteins, 2,065 were found to be common among all of the three conditions (Fig. 2 B).

Comparison of protein abundance was evaluated by spectral counting using QuasiTel software (Li et al., 2010), which predicted statistically significant differences in the spectral count numbers for detected proteins between control and KD exosomes for only 22 out of the 2,102 proteins (Table S1). Because QuasiTel bases part of its significance estimate on spectral count variability across biological replicates, only proteins demonstrating sufficient consistency in detection enable confident quantitative comparisons. Thus, if a substantial number of differentially packaged proteins exist, they are below our ability to reliably quantitate them using this technology platform. As a measure of variability, the coefficient of variation within a group of biological replicates was examined for control and KD-derived exosomes (Table S1). As expected, proteins with lower spectral counts have higher coefficient of variation values. We also performed WB analyses for candidate proteins, comparing equal numbers of control and cortactin-KD exosomes (Fig. 2, C and D). As expected from the spectral count analysis, there were no significant differences in EGFR levels in the exosome preparations. In addition, although our Quasitel analysis identified collagen I and MMP2 as potentially significantly different cargoes between control and KD exosomes (Table S1), they were present at equivalent levels by WB analysis. Notably, MMP2 is a bona fide exosome component as it is not present in the supernatant of conditioned media after 100,000 g centrifugation to pellet exosomes (Fig. 2 E). These data suggest that cortactin controls exosome number, but not cargo content.

Cortactin regulates MVE trafficking

Secretion of exosomes could be regulated at several points, including exosome biogenesis within early endosomes and trafficking and secretion of MVEs. Previously, we showed that cortactin-KD cells have a defect in late endosomal (LE) trafficking and accumulate enlarged LE/lysosomal (Lys) compartments (Sung et al., 2011; Kirkbride et al., 2012; Hong et al., 2015). Here, we confirmed that SCC61 cortactin-KD cells contain enlarged LE/Lys hybrid organelles by TEM of 50-nm cell sections (Fig. 3 A; Kirkbride et al., 2012). In addition, we observed intact MVE in both control and cortactin-KD cells (Fig. 3 A). We also observed a few vacuole-like structures (Fig. 3 A and Fig. S2 D, marked with a "V" in KD cell images), which in KD cells could represent endosomes that are unable to form intraluminal vesicles (Baietti et al., 2012; Ghossoub et al., 2014). To test this possibility, MVE were labeled by allowing control and KD cells to bind and endocytose anti-CD63 antibody conjugated to horseradish peroxidase before fixation, development with DAB, and processing for TEM. In both control and cortactin-KD cells, DAB staining was concentrated in MVE structures but did not
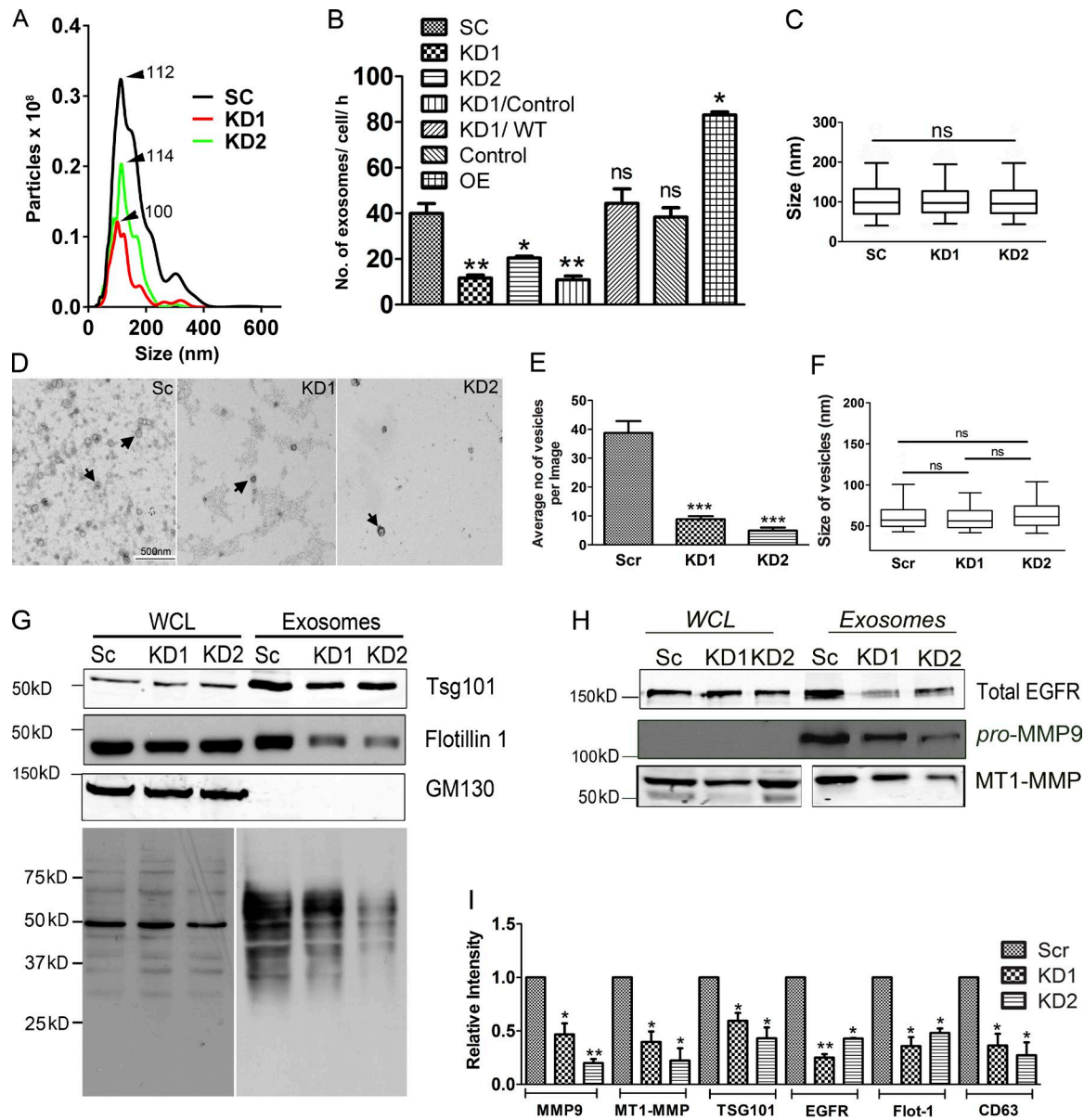
Figure 1. **Cortactin levels control exosome secretion.** Exosome preparations purified from equal numbers of cells were analyzed. (A) Representative nanoparticle tracking analysis (NTA) traces of exosomes derived from SCC61 control (SC) and cortactin knockdown (KD1 and KD2) cells, normalized to cell number. (B) Quantification from $n = 3$ independent experiments. Rescue constructs indicated after the slash (/) for empty vector (control) or WT (wild-type) cortactin. OE, cortactin overexpression in parental cells. Western blots (WBs) of cortactin levels in KD and OE cells shown in Fig. S1 and of KD/rescue cells in Fig. 5. (C) Quantitation of vesicle size by NTA. (D) Representative TEM images of exosome preparations from scrambled control (Sc) and cortactin knockdown (KD1 and KD2) cells. (E) Quantification of mean exosome number per EM image. (F) Size of vesicles ≥ 40 nm quantitated from EM images. Quantitations in E and F from 28–30 images per condition, $n = 3$ independent experiments (total number of vesicles across all images = 1,146 for control, 277 for KD1, and 129 for KD2). (G and H) Representative WBs of control and cortactin-KD whole-cell lysates (WCL) and exosomes (Exo). WCLs are loaded according to equal protein, whereas exosomes are loaded according to cell number. (I) Quantitation of WB. $n = 3$ independent experiments. Parametric data plotted as bar graphs, mean ± SE, and analyzed for statistical significance using a Student's t test. Nonparametric data graphed with box and whiskers plots, where the line indicates median, the box indicates 25–75th percentile and the whiskers indicate 5–95th percentile, and analyzed by Mann–Whitney U test. ns, not significant; *, $P < 0.05$; **, $P < 0.01$; ***, $P < 0.001$.

label the empty vacuoles (Fig. S2, A–D). These data suggest that the empty vacuoles are not pre-MVE structures and that cortactin is unlikely to affect exosome biogenesis.

To further examine the role of cortactin in exosome biogenesis, we used a light microscopy assay in which expression of Rab5a Q79L promotes enlargement of early-to-late transitioning endosomes (Stenmark et al., 1994; Baietti et al., 2012). Within those enlarged endosomes, intraluminal vesicle accumulation is easily visualized by immunostaining for the exosome marker CD63 (Baietti et al., 2012; Ghossoub et al., 2014). Analysis of confocal images revealed that control and cortactin-KD cells had an equivalent percent of GFP-Rab5a Q79L-positive endosomes filled with luminal CD63 (Fig. 3, B and C). Together with our finding that cortactin affects the number, but not cargo content, of exosomes (Figs. 1 and 2 and Fig. S1) and that MVEs are present in cortactin-KD cells (Fig. 3 A and Fig. S2, A–D), these data indicate that cortactin does not affect exosome biogenesis.
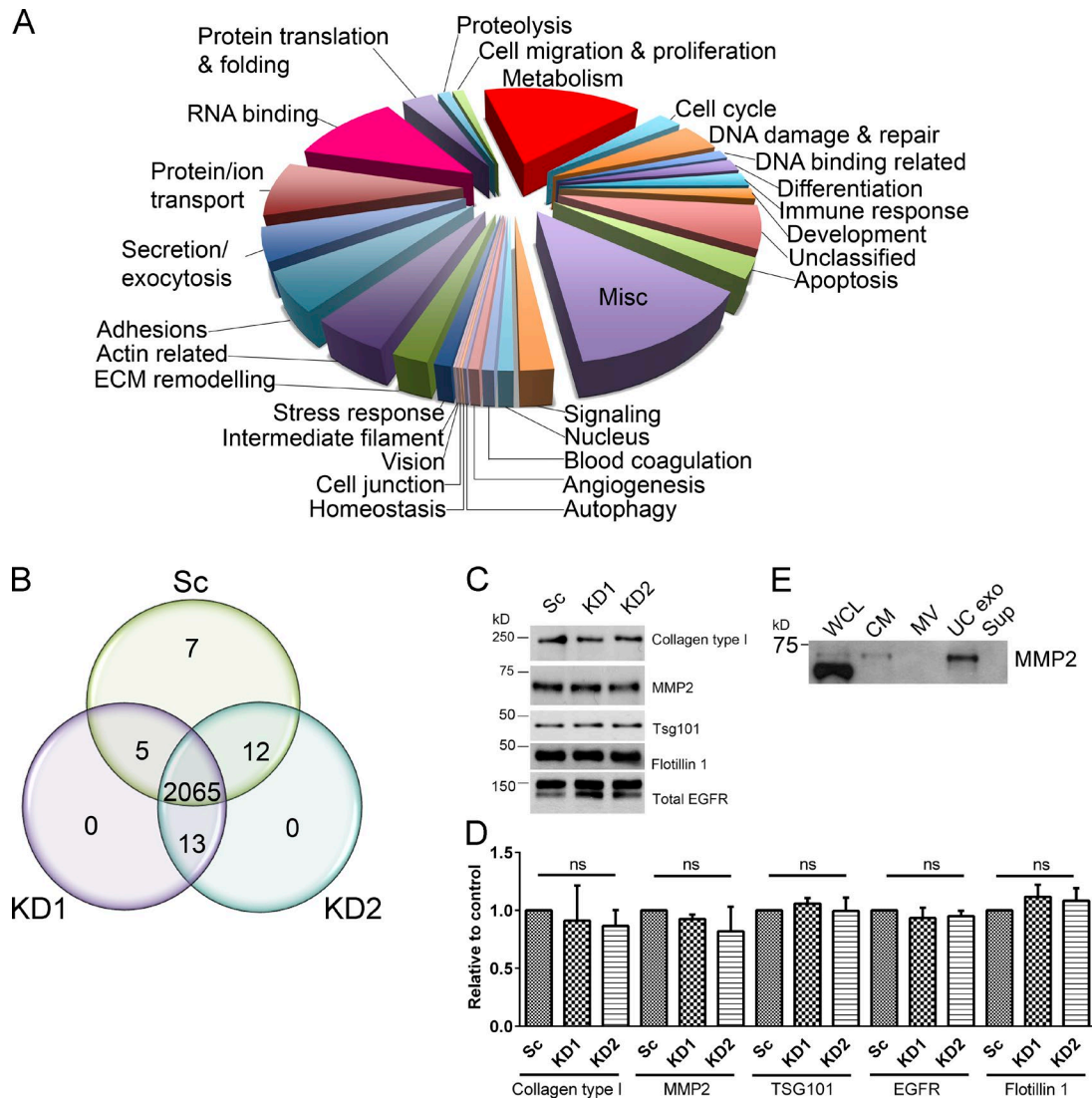
Figure 2. **Cortactin does not control exosome cargo selection.** (A) Classification of proteins identified in equal numbers of exosomes that are common between SCC61-control (Sc), cortactin-KD1 (KD1) and cortactin-KD2 (KD2) cells based on their UniProt identified function. (B) Venn diagram representing the presence, absence, or overlap of proteins identified through LC-MS/MS in exosomes purified from the indicated cell lines. Proteomics data $n = 3$ independent experiments. (C) WB analysis of proteins present in an equal number of exosomes purified from control and cortactin-KD cells. (D) Quantitation of WB. $n = 3$. Bar graphs = mean ± SE. Significance analyzed by Student's t test. ns, not significant. (E) WB analysis of MMP2 in whole-cell lysate (WCL), conditioned media (CM), microvesicle (MV), exosomes (UC exo), and supernatant (Sup) from the UC exo centrifugation step. Representative of $n = 3$ experiments.

In both the GFP-RabQ79L experiments (Fig. 3 B) and in separate immunostaining experiments (Fig. 3, D–F), cortactin-KD cells exhibited enlarged CD63-positive endosomal structures but did not change the total cell area occupied by CD63-positive compartments. In addition, confocal imaging of cells expressing GFP-CD63 and the exosome cargo mCherry-MMP9 revealed that MMP9 localized within CD63-positive endosomes in both control and cortactin-KD cells (Fig. S3 A). These data suggest that cortactin affects MVE trafficking downstream of exosome biogenesis, such as transport to or docking at the PM.

To determine whether cortactin controls MVE transport, we analyzed the dynamics of GFP-CD63–positive endosomes by confocal imaging. We found that many GFP-CD63–positive endosomes were transported to and from the cell periphery in fast, directional movements consistent with microtubule-based

transport (Fig. S3 B and Video 1). Dynamic tracking analysis revealed that cortactin-KD cells contained fewer moving GFP-CD63–positive endosomes compared with control cells (Fig. S3, B and C). In contrast, a similar number of moving GFP-CD63–positive endosomes was observed in cortactin-OE and control cells. To analyze MVE speed, diffusion coefficients (mean square displacement/time, D) were calculated for individual endosomes. For both fast-moving (>3 μm²/s) and slow-moving (<3 μm²/s) endosomes, there was no significant difference in D among control, KD, or overexpressed cells (Fig. S3, D and E). Although KD cells have a decrease in the number of moving endosomes, the lack of effect of cortactin OE on MVE transport while affecting exosome secretion suggests that cortactin controls an additional step in the exosome secretion pathway.

In addition to MVE transport, exosome secretion could be affected by alterations in MVE docking or fusion with the
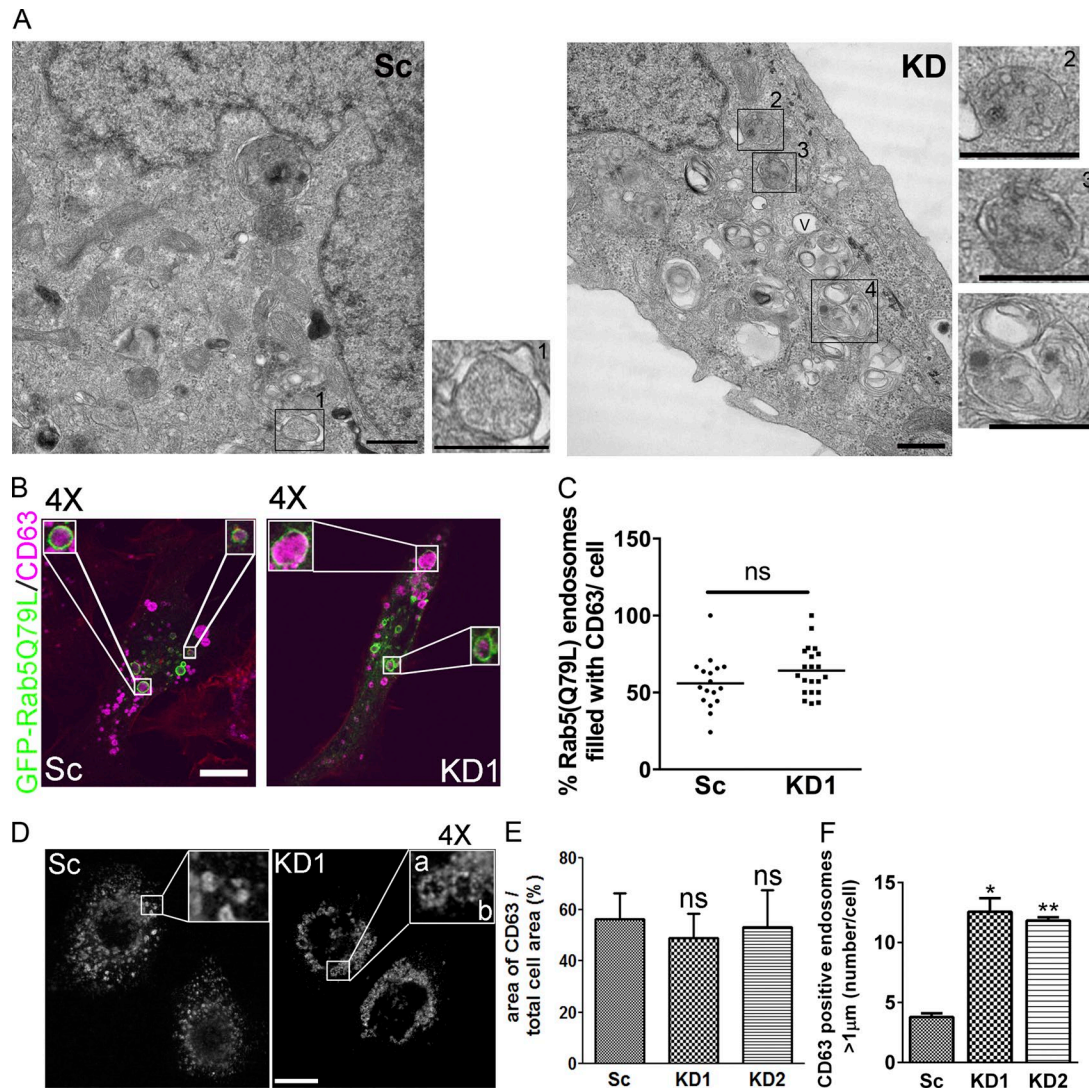
Figure 3. **Cortactin affects MVE trafficking downstream of biogenesis.** (A) Representative TEM images of 50-nm cell sections for SCC61-control (Sc, left) and cortactin-KD (KD, right) cells. MVEs (seen in zooms) from control (1) and cortactin-KD cells (2 and 3). V, empty vacuole like structure. Example LE/Lys hybrid organelle shown in zoom 4. Bars, 500 nm. (B) Representative confocal micrographs of SCC61 control (Sc) and cortactin-KD1 (KD1) cells transiently transfected with GFP-Rab5Q79L (green) and stained for endogenous CD63 (purple) along with actin filaments (rhodamine phalloidin, red). Insets show 4× zooms. Bar, 15 μm. (C) Quantitation of percent GFP-Rab5Q79L positive endosomes filled with CD63. $n \geq 17$ cells per condition $n \geq 3$ independent experiments. Lines show mean values. (D) Representative confocal images of immunostained CD63. Bar, 10 μm. Insets (4× zooms). a and b are two example endosomes in a KD cell. (E) Quantitation of CD63-positive area/cell area. (F) Quantitation of the number of large (>1 μm) CD63-positive endosomes per cell. $n \geq 31$ cells per condition $n \geq 3$ independent experiments. Bar graphs represent mean ± SE. ns, not significant; *, $P < 0.05$; **, $P < 0.01$. Student's *t* test used to determine statistical significance.

PM. To test this possibility, total internal reflection fluorescence (TIRF) microscopy was performed to visualize MVE docking at the basal surface of cells. TIRF microscopy of cells immunostained with an antibody against CD63 revealed that both cortactin-KD and Rab27a-KD cells exhibited a reduced number of MVEs at the cell–substrate interface compared with control cells (Fig. 4, A and B; and Fig. S4 A). Note that the large CD63-positive endosomes in the center of cortactin-KD cells are likely immature LE/Lys hybrid organelles, as previously characterized (Kirkbride et al., 2012). Conversely, cortactin-overexpressed cells exhibited an increased number of CD63-positive puncta at the cell–substrate interface.

To further examine MVE docking, live TIRF microscopy was performed on cells expressing GFP-CD63 (Fig. 4, C–E; Fig. S4 B; and Videos 2, 3, 4, and 5). Because docked vesicles are immobile, live TIRF microscopy imaging is ideal to assess alterations in vesicle docking. Rab27a-KD cells were used as a positive control, because the role of Rab27a in MVE docking was recently defined using this approach (Ostrowski et al., 2010). In cells expressing GFP-CD63, the profile of CD63-positive endosomes present at the basal surface was similar to that of immunostained cells, with a decrease in cortactin- and Rab27a-KD cells and an increase in cortactin-overexpressed cells compared with control (Fig. 4 C). Furthermore, analysis of movies revealed that Rab27a- and cortactin-KD cells exhibited a decrease in both the percentage and number of MVEs that were immobile for ≥ 5 s (Fig. 4, D and E; and Videos 2, 3, 4, and 5). Conversely, cortactin-overexpressed cells exhibited no increase in the percentage of immobile MVEs; however, because of the overall increase in the number of MVEs at the PM,
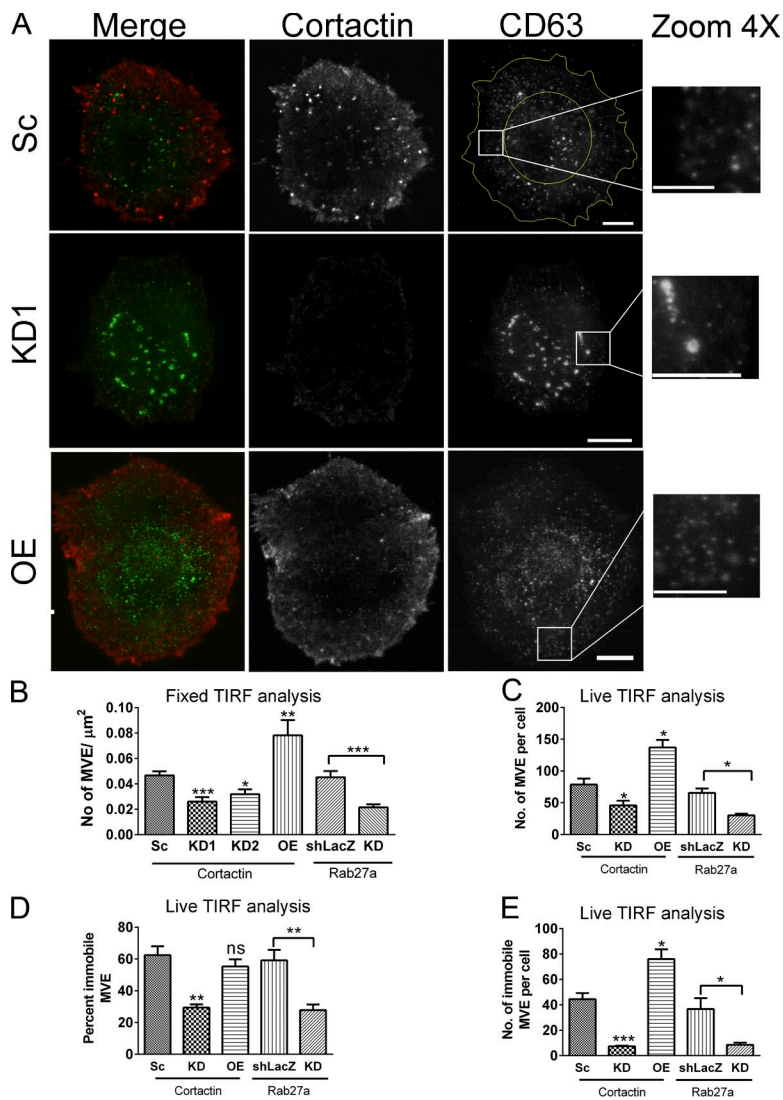
Figure 4. **Cortactin controls MVE docking at the PM.** (A–E) TIRFM of fixed and live cells. For analyses of TIRF images in B–E, the center of the cell (demarcated by the yellow circle in A) was excluded. (A and B) Cells were immunostained for CD63 (green) and cortactin (red). (A) Representative images. Bars: (main images) 10 µm; (zoom) 5 µm. Note increased vesicle number in Sc and OE cells compared with KD in zooms. (B) Number of CD63-positive vesicles per square micrometer cell area. $n \geq 20$ cells per condition from three or more independent experiments. (C–E) Cells were transiently transfected with GFP-CD63 and imaged live. Individual vesicles were tracked to yield quantitation of total number of MVEs (C), percentage of immobile MVEs (D), and number of immobile MVEs (E) present at the PM. See Fig. S4 B for representative images. $n \geq 8$ cells for each condition and $n \geq 3$ independent experiments. Bar graphs represent mean ± SE. ns, not significant; *, $P < 0.05$; **, $P < 0.01$; ***, $P < 0.001$. Student's t test determined statistical significance.

cortactin-overexpressed cells exhibited a large increase in the number of immobile MVEs per cell. In separate experiments using a deeper TIRF angle to allow tracking of MVE movement near the plane of the membrane (Ostrowski et al., 2010), individual MVE movement was tracked and diffusion coefficients were calculated for each MVE as a measurement of motility (Videos 6, 7, 8, and 9; and Fig. S4, C and D). As previously reported (Ostrowski et al., 2010), MVE motility in the TIRF field was significantly increased in Rab27a-KD cells, indicating a docking defect (Fig. S4 D and Video 9). Similarly, MVE motility was increased in cortactin-KD cells compared with control cells. Although the MVE in cortactin-overexpressed cells were slightly less mobile than control cell MVEs (Fig. S4 D), the difference was not statistically significant, potentially because of the very low mobility of MVEs in both cell types. Overall, these data indicate that cortactin controls MVE docking at the PM.

Interaction of cortactin with the Arp2/3 complex and F-actin is critical for exosome secretion

Cortactin is a unique branched actin regulator that controls actin dynamics by linking the actin nucleating Arp2/3 complex to actin filaments via its N terminus (Kirkbride et al., 2011). Cortactin also binds diverse cytoskeletal, membrane trafficking, and signaling proteins at its C terminus. To understand the molecular mechanism by which cortactin controls exosome secretion, we performed a structure–function analysis of cortactin binding interactions required for exosome secretion. shRNA-insensitive WT cortactin or cortactin proteins with mutations in the binding sites for the Arp2/3 complex (W22A), actin filaments (Δ4RP), or SH3 domain–binding partners (W525K) or in the Src phosphorylation sites (3Y; Huang et al., 1998; Weed et al., 2000; Kinley et al., 2003; Martinez-Quiles et al., 2004) were expressed in cortactin-KD1 cells (Fig. 5, A and B). The number of exosomes secreted by each cell type was quantitated by NanoSight NTA (Fig. 5 C). Expression of WT cortactin, SH3 domain (W525K), or Src phosphorylation site (3Y) mutants fully rescued exosome secretion by KD cells. However, expression of Arp2/3 complex (W22A) or actin filament (Δ4RP) binding mutants did not rescue KD cell defects, suggesting that cortactin controls exosome secretion through regulating branched actin dynamics. Consistent with this hypothesis, inhibition of the Arp2/3 complex with the drug CK-666 reduced exosome secretion at concentrations that do not affect cell viability (Fig. 5, D and E).
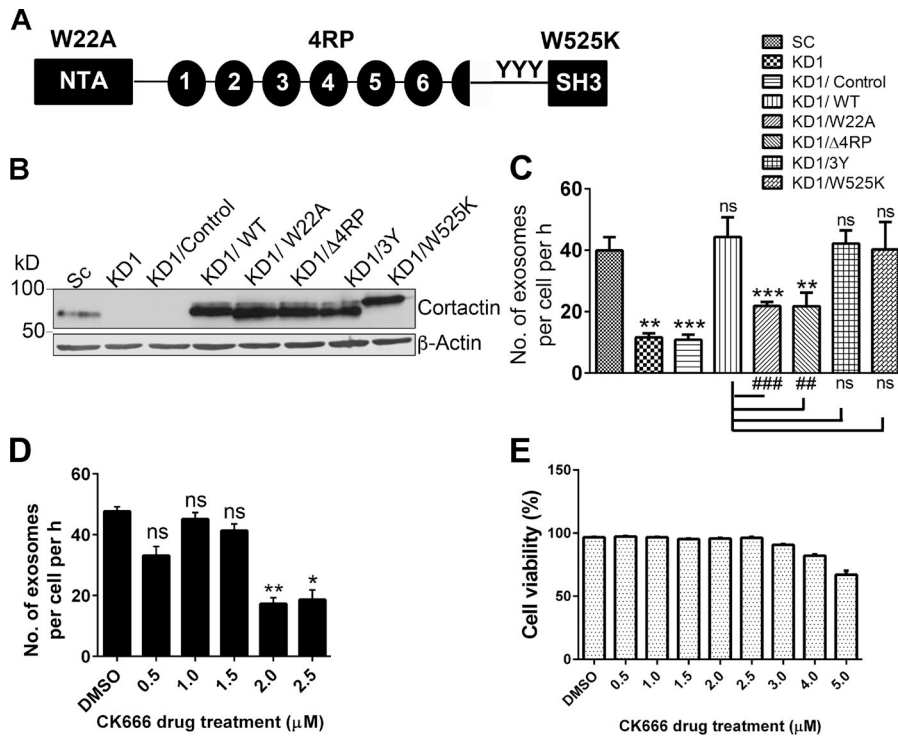
A

W22A 4RP W525K

NTA — ①②③④⑤⑥ — YYY SH3

B

kD

Sc KD1 KD1/Control KD1/ WT KD1/ W22A KD1/Δ4RP KD1/3Y KD1/W525K

100

50

Cortactin

β-Actin

C

Legend:
SC
KD1
KD1/ Control
KD1/ WT
KD1/W22A
KD1/Δ4RP
KD1/3Y
KD1/W525K

No. of exosomes per cell per h (0–60)

ns, **, ***, ***, **, ns, ns; ###, ##, ns, ns

D

No. of exosomes per cell per h (0–60)

ns ns ns ** *

DMSO 0.5 1.0 1.5 2.0 2.5

CK666 drug treatment (μM)

E

Cell viability (%) (0–150)

DMSO 0.5 1.0 1.5 2.0 2.5 3.0 4.0 5.0

CK666 drug treatment (μM)

Figure 5. **Binding of cortactin to Arp2/3 complex and F-actin is critical for exosome secretion.** (A) Cortactin domain structure indicating mutation sites: W22A, prevents Arp2/3 binding; NTA, N-terminal acidic Arp2/3-binding domain; Δ4RP, deletion of fourth repeat in tandem repeats region prevents F-actin binding; 3Y, Src kinase phosphorylation sites (tyrosines 421, 466, and 482 mutated to phenylalanine); W525K, prevents binding to SH3 domain binding partners. (B) WB analysis of cortactin wild-type (WT) and mutant (W22A, Δ4RP, 3Y, and W525K) re-expressed proteins in cortactin-KD1 cell lines. Control indicates empty vector for rescue constructs. (C) NTA quantitation of exosomes secretion rate of indicated cell lines. $n \geq 3$ independent experiments. (D) NTA quantitation of exosomes secreted from SCC61 cells in the presence of DMSO or various concentrations of CK666 (Arp2/3 inhibitor) for 24 h. $n \geq 3$ independent experiments. (E) Cell viability for SCC61 cells treated with DMSO or CK666 for 48 h. $n \geq 3$ independent experiments. Bar graphs represent mean ± SE. *, $P < 0.05$; **, $P < 0.01$; ***, $P < 0.001$ indicates comparison to Sc control; ##, $P < 0.01$; ###, $P < 0.001$ indicates comparison to KD1/WT rescue. ns, not significant. Analyzed by Student's t test.

Cortactin, Rab27a, and coronin 1b coordinately control cortical branched actin dynamics and exosome secretion

Invadopodia are branched actin-rich structures that are regulated by cortactin and can serve as docking sites for MVEs (Kirkbride et al., 2011; Hoshino et al., 2013b). Our TIRF experiments revealed that both Rab27a and cortactin control MVE docking, presumably by different mechanisms, respectively tethering MVE to existing docking sites (Ostrowski et al., 2010) and creating new docking sites via branched actin assembly (Kirkbride et al., 2011). To test this model, we knocked down Rab27a in cortactin-overexpressed cells and quantitated the rate of exosome secretion (Fig. 6, A and B). Contrary to our expectation that loss of Rab27a should reverse the enhanced exosome secretion of cortactin-overexpressed cells, we found no change in exosome secretion. These data suggest that cortactin overexpression may compensate for the lower Rab27a levels and potentially work in the same process.

Although control of actin assembly has not been highly studied for Rab27a, Rab27a has been reported to regulate both cortical and endosome-associated actin (Desnos et al., 2003; Kimura et al., 2010; Yokoyama et al., 2011; Singh et al., 2013). Notably, two studies demonstrated that Rab27a can control localization of the actin-binding protein coronin to actin assemblies (Kimura et al., 2010; Yokoyama et al., 2011). Because coronin directly antagonizes cortactin at actin branch points (Cai et al., 2008), such a mechanism could explain compensatory interactions between cortactin and Rab27a. To test whether Rab27a controls coronin localization to invadopodial branched actin assemblies, control, Rab27a-KD, cortactin-overexpressed, and cortactin-overexpressed/Rab27a-KD cells were cultured on FITC-fibronectin (FN)/gelatin plates before immunostaining for the common epithelial isoform coronin 1b (Fig. 7, A–C). Invadopodia are evident as actin-rich puncta that colocalize with dark degraded matrix areas (Weaver, 2008). As we previously reported (Hoshino et al., 2013b), Rab27a-KD decreased
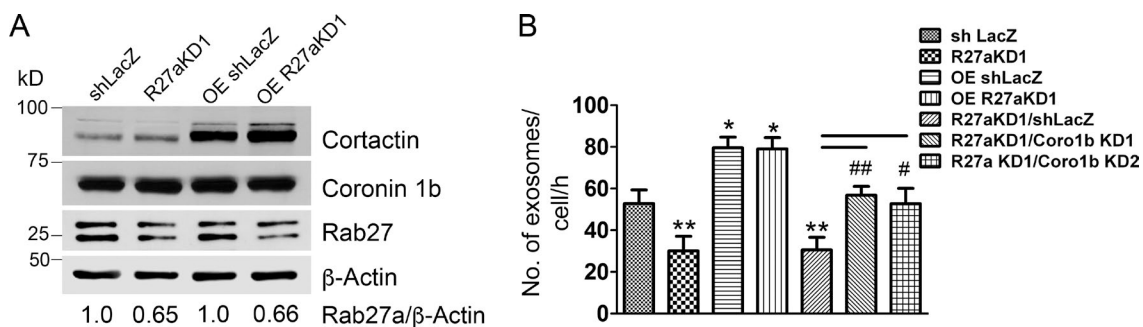
A

kD

shLacZ R27aKD1 OE shLacZ OE R27aKD1

100

75

Cortactin

Coronin 1b

25

Rab27

50

β-Actin

1.0 0.65 1.0 0.66 Rab27a/β-Actin

B

Legend:
sh LacZ
R27aKD1
OE shLacZ
OE R27aKD1
R27aKD1/shLacZ
R27aKD1/Coro1b KD1
R27a KD1/Coro1b KD2

No. of exosomes/cell/h (0–100)

**, *, *, **, ##, #

Figure 6. **Cortactin overexpression compensates for Rab27a loss.** (A) WB analysis of SCC61 control (shLacZ), Rab27a-KD1 (R27aKD1), cortactin-overexpressed (OE shLacZ), and cortactin-overexpressed cells knocked down for Rab27a (OE R27aKD1). Numbers indicate Rab27 levels normalized to β-actin levels, as a fraction of control. (B) NTA quantitation of exosomes secreted from the indicated cell lines. $n \geq 3$ independent experiments. Bar graphs = mean ± SE. *, $P < 0.05$; **, $P < 0.01$ compared with shLacZ; #, $P < 0.05$; ##, $P < 0.01$ compared with R27aKD1/shLacZ, analyzed by Student's t test.
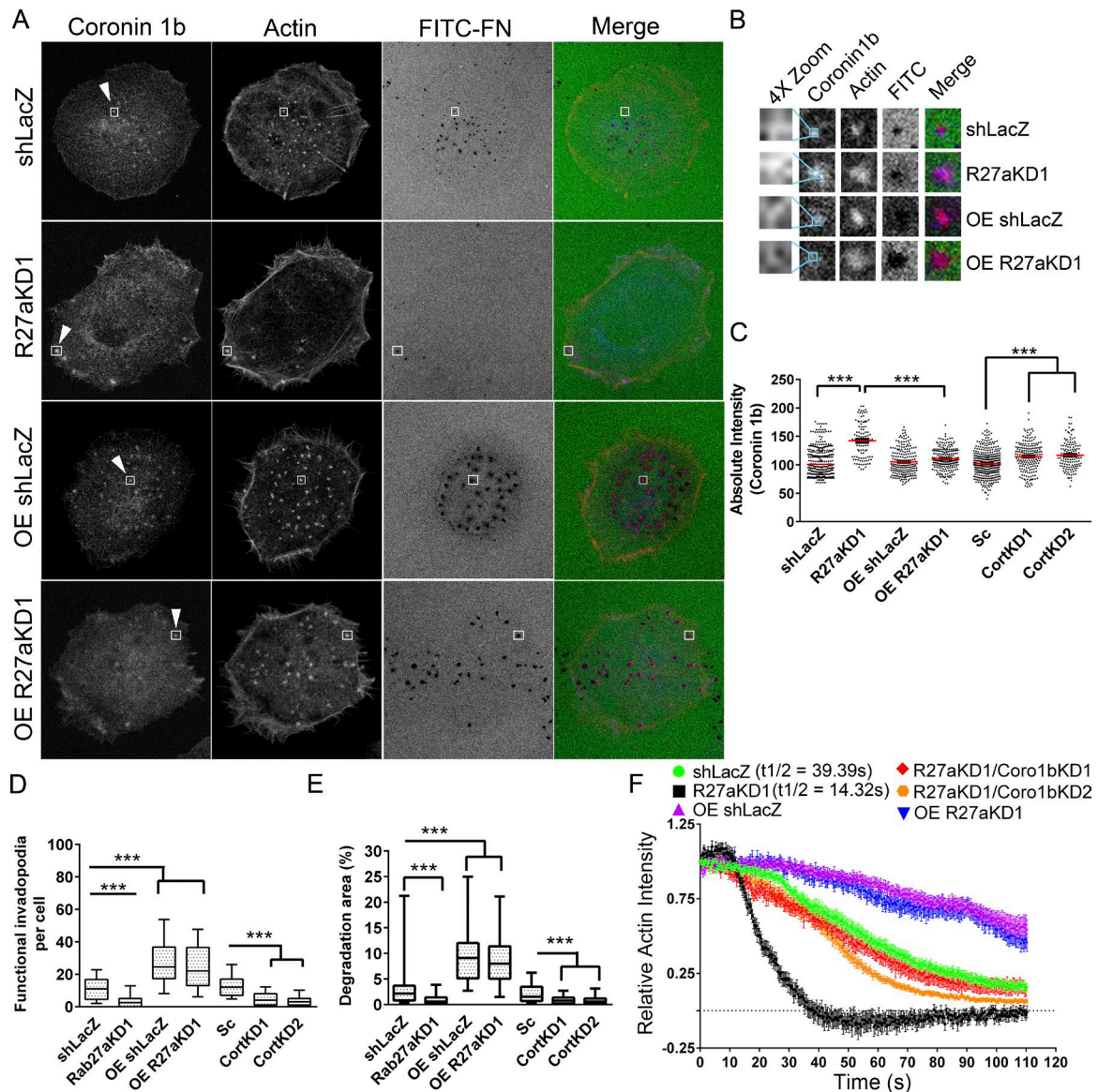
Figure 7. **Cortactin, Coronin 1b, and Rab27a coordinately control invadopodial actin dynamics.** (A) Representative confocal immunofluorescence images showing localization of coronin 1b and actin to invadopodia. ECM degradation evident as dark spots in FITC-FN images. Fluorescence levels of the images were enhanced equally across all images for visualization only, not for quantitation. Bar, 15 μm. Boxes outline example invadopodia and are shown in B. (B and C) Quantitation of the absolute intensity of coronin 1b at invadopodia was measured using 4 × 4–pixel boxes. Representative blue 4 × 4–pixel boxes are shown within the coronin 1b zooms and are further zoomed 4× and shown on the left (B). Quantitations shown in C. $n \geq 5$ invadopodia per cell from ≥35 cells per condition, $n \geq 3$ independent experiments Scatterplot with median is plotted. Analyzed by Mann–Whitney U test. (D and E) Quantification of functional invadopodia per cell and ECM degradation area percentage. Box and whisker plots with median shown as a line, box indicates 25–75th percentile and whiskers indicate 5–95th percentile. $n \geq 3$ independent experiments. ***, $P < 0.001$, determined by Mann–Whitney U test. (F) Actin turnover in invadopodia after 10 μM latrunculin A (LatA) treatment was assessed by live TIRF imaging. See also Video 10. Actin fluorescence intensity at invadopodia after LatA treatment is plotted. Five or more invadopodia per cell were quantitated for ≥10 cells for each condition; $n \geq 3$ independent experiments.

invadopodia number and activity (Fig. 7, D and E). Consistent with previous studies of endosome and phagosome actin (Kimura et al., 2010; Yokoyama et al., 2011), Rab27a-KD cells had increased intensity of coronin 1b at the remaining invadopodial actin puncta (Fig. 7, B and C). This increase did not occur in cortactin-overexpressed Rab27a-KD cells, suggesting that cortactin antagonizes coronin binding to invadopodial branched actin. Consistent with that model, cortactin-KD cells immunostained for coronin 1b exhibited increased coronin fluorescence intensity at invadopodia, despite no change in actin fluorescence intensity (Fig. 7 C; and Fig. S5, B–D). Likewise, KD of coronin 1b in Rab27a-KD cells led to increased cortactin

fluorescence intensity at invadopodia, without affecting actin intensity (Fig. S5, E–H). Coronin 1b-KD in Rab27a-KD cells also led to an increase in both invadopodia activity (Fig. S5 I) and exosome secretion (Fig. 6 B).

To test whether Rab27a and cortactin affect invadopodial actin stability, control, Rab27a-KD, cortactin-overexpressed and cortactin-overexpressed Rab27a-KD cells were transiently transfected with the actin marker EGFP-F-Tractin. 10 μM latrunculin A was added to cells, and live TIRF microscopy was performed (Video 10). Because latrunculin A prevents new actin polymerization by sequestering monomeric actin (Morton et al., 2000), only disassembly of dynamic actin structures

is observed (Hong et al., 2015). EGFP-F-Tractin fluorescence was rapidly lost over time in control cells, with a $t_{1/2}$ of actin intensity loss of 39 s (Fig. 7 F and Video 10). Invadopodial actin disassembled faster in Rab27a-KD cells than in control cells ($t_{1/2}$ = 14 s). In both cortactin-overexpressed and cortactin-overexpressed Rab27a-KD cells, the invadopodial actin was much more stable and did not fully disassemble by the end of the movie (Fig. 7 F and Video 10). Because Rab27a controls coronin localization to invadopodia (Fig. 7, A–C), we also tested whether coronin KD could reverse the rapid actin disassembly that occurs in Rab27a-KD cells. Indeed, KD of coronin 1b in Rab27a-KD cells led to more stable actin dynamics, with a similar disassembly rate to that of control cells (Fig. 7 F). These data demonstrate that Rab27a and cortactin coordinately promote cortical actin stability and exosome secretion; coronin antagonizes these activities.

Cortactin-dependent cancer phenotypes are controlled by exosomes

Cortactin controls diverse oncogenic traits, including serum and anchorage independence and cellular invasiveness (Timpson et al., 2007; Weaver, 2008; Clark et al., 2009; Kirkbride et al., 2011). To test the contribution of exosome secretion to cortactin function in cancer cell aggressiveness, we tested whether adding ultracentrifuge (UC)-purified exosomes to cortactin-KD cells could rescue defects in serum independent growth and invasion. For serum-independent growth, control and cortactin-KD1 cells were incubated for 4 d in serum-free, growth factor–free media in the presence or absence of 50 µg/ml exosomes purified from control or cortactin-KD1 cells, before cell counting. This exosome concentration was chosen based on a previous range of 25–100 µg/ml shown to modulate cell proliferation and migration (Lee et al., 2013) and represents 35 × 10^8 exosomes per well. As a positive control, Rab27a-KD cells were also tested (Ostrowski et al., 2010; Bobrie et al., 2012). As previously reported (Clark et al., 2009), cortactin-KD cells proliferate less than control cells under serum-independent conditions (Fig. 8 A, left). Consistent with an important role for exosomes in serum-independent growth, Rab27a-KD cells also proliferated less than control cells (Fig. 8 A, right). However, in the presence of UC exosomes, defects in serum-independent growth of cortactin- or Rab27a-KD cells were fully rescued (Fig. 8 A). Consistent with our data that cortactin primarily controls exosome number and not cargo content (Figs. 1 and 2), exosomes purified from cortactin-KD cells rescued cortactin-KD cell defects to the same extent as an equivalent concentration of control exosomes. Likewise, 50 µg/ml UC-exosomes purified from control or Rab27a-KD cells had equivalent bioactivity.

For invasion, 50 µg/ml control or KD UC exosomes was mixed with control or cortactin-KD cells and added to the top of Matrigel-coated Transwell invasion chambers. The proteinase inhibitor GM6001 was used as a positive control to prevent invasion of control cells (Fig. 8 B, left). After 48 h, cell invasion to the bottom of the filter was assessed. Similar to serum independence, defects in Transwell invasion of cortactin-KD and Rab27a-KD cells were equivalently rescued by exosomes derived from either control or KD cells (Fig. 8 B).

Because UC preparations of exosomes can contain protein aggregates (Thery et al., 2006), we further purified UC exosomes by density gradient (DG) sedimentation into a 5–40% iodixanol gradient. WB analysis revealed that exosomes were primarily present in fraction 7 (Fig. 8 C, DG exosomes),

consistent with their expected density of ∼1.11 g/ml (Greening et al., 2015). NTA analysis revealed a similar peak size of DG exosomes to that of UC exosomes, although with a slightly more narrow size distribution (Fig. 8 D). TEM images of negatively stained DG exosomes confirmed typical exosome morphology and revealed less background staining than UC exosomes (compare Fig. 8 E to Fig. 1 D).

To determine whether DG exosomes could rescue serum-independent growth defects similarly to UC exosomes, cortactin-KD cells were cultured in serum free media in the presence of various concentrations of UC or DG exosomes for 96 h. Based on the numbers of UC exosomes purified from 48 h conditioned medium, we estimate that control cells secrete ∼40–50 exosomes per cell per hour (Fig. 1 B). This estimate does not account for exosome uptake by cells or loss during purification. Based on that rate, we calculated that control cells should secrete ∼120 × 10^6 exosomes over a period of 96 h (Fig. 8 F). Hence, we treated cortactin-KD cells with doses ranging from 12 × 10^6 to 120 × 10^6 exosomes for the 96-h assay (Fig. 8 G). MV were used as a negative control and tested at the highest dose. Serum-independent growth defects of KD cells were fully rescued by coincubation of cells with either UC or DG exosomes at both the 84 × 10^6 and 120 × 10^6 vesicle concentrations. By contrast, there was no effect of MVs purified from the same conditioned media (Fig. 8 G). Similarly, both UC and DG exosomes rescued Transwell invasion defects of KD cells, whereas MVs had no effect (Fig. 8 H). Although there was a trend toward increased efficacy of UC exosomes in this assay, the differences were small and not statistically significant. Because the Opti-MEM media that we use to prepare conditioned medium and thus exosomes contains growth factors, we also tested whether exosomes purified from growth factor–free media with a 70 min UC step can rescue serum-independent growth of cortactin-KD cells. Indeed, exosomes purified this way did rescue serum-independent growth, at similar concentrations to UC or DG exosomes purified from Opti-MEM (Fig. 8, compare I and G). We also tested whether the key invadopodial proteinase MT1-MMP is an essential exosome cargo for promoting Transwell invasion. Cortactin-KD cells were incubated with UC exosomes purified from either control or MT1-MMP-KD cells in Transwell invasion chambers. Surprisingly, we found equivalent activity of control and MT1-MMP-KD exosomes in rescuing cortactin-KD cell Transwell invasion (Fig. 8, J and K). These data suggest that other exosome cargoes are either more important or compensate for MT1-MMP function in this assay.

Discussion

Secreted exosomes control multiple aspects of cellular function and communication (Théry, 2011; Raposo and Stoorvogel, 2013; Yáñez-Mó et al., 2015). However, the current understanding of cellular and molecular mechanisms that control exosome secretion is limited. We find that the cytoskeletal protein cortactin controls secretion of exosomes but has little effect on their cargo content. Live imaging revealed that cortactin controls both LE trafficking and MVE docking. Structure–function analyses identified binding of cortactin to the Arp2/3 complex and actin filaments as critical for exosome secretion. Further investigation revealed that cortactin, Rab27a, and coronin 1b coordinately control branched actin dynamics at cortical invadopodial MVE docking sites and exosome secretion (Fig. 9).
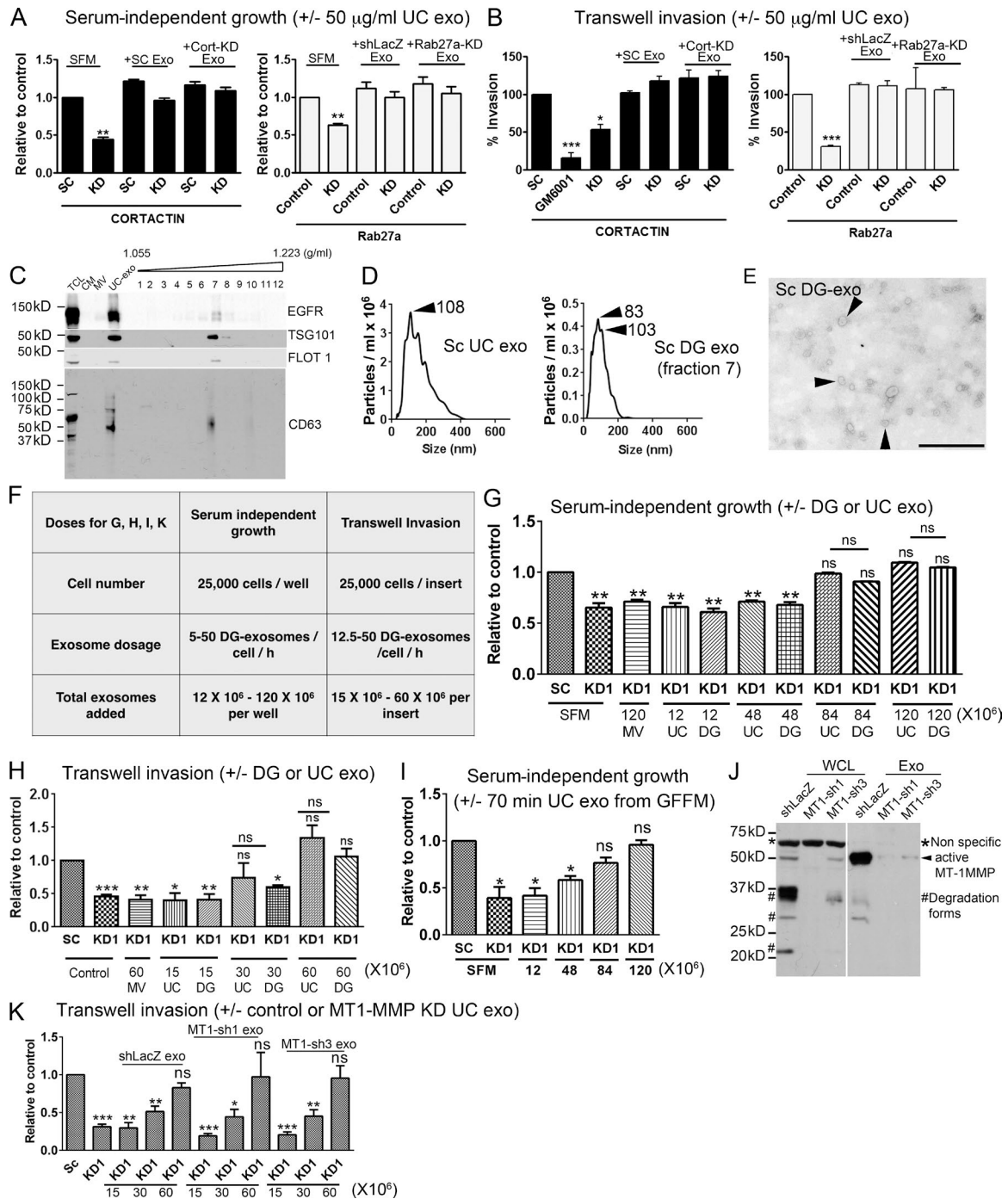
Figure 8. **Cortactin-dependent oncogenic phenotypes are controlled by exosomes.** (A) Cells were cultured in serum-free medium (SFM) or SFM supplemented with equal concentrations (50 µg/ml, calculated to be 35×10^8 exosomes per well) of control (+SC Exo or +shLacZ Exo) or cortactin-KD or Rab27a-KD UC exosomes, as indicated, for 4 d. Relative number of cells compared with control cells (SFM condition) shown as mean ± SE, $n = 3$ independent experiments with triplicate wells. (B) 48 h invasion across Matrigel-coated invasion chambers in the presence or absence of equal concentrations (50 µg/ml) control or KD UC exosomes. Cells per image were averaged for each replicate. $n = 3$ independent experiments with duplicate wells. (C) WB of exosome markers in control and cortactin-KD total cell lysates (TCL), conditioned medium (CM), microvesicles (MV), UC exosomes, or density gradient (DG) fractions 1–12. Note the presence of exosome markers in fraction 7. (D) Representative (from $n = 3$) NTA size distribution traces of UC exosomes and DG exosome fraction 7. (E) Representative TEM images of DG exosome fraction 7 preparation from scrambled control (Sc) cells. (F) Table outlining exosome doses used in experiments G–I and K. (G) Serum-independent growth of control (Sc) and cortactin-KD1 cells cultured in the presence of various concentrations ($12–120 \times 10^6$, indicated below) of UC or DG exosomes, or MVs derived from control cells. $n = 3$ independent experiments with triplicate wells. (H) 48 h invasion across Matrigel-coated invasion chambers in the presence of various concentrations of control cell UC or DG exosomes, or MV. $n = 3$ independent experiments with duplicate wells. (I) Serum-independent growth of control (Sc) and cortactin-KD1 cells cultured in the presence or absence of exosomes purified by 70 min ultracentrifugation from Sc cells cultured in growth factor–free medium (GFFM). $n = 3$ independent experiments with triplicate wells. (J) WBs of whole-cell lysate and UC exosomes derived from SCC61 cells shLacZ (control) and MT1-MMP knockdown (MT1-sh1 and sh3). Note active MT1-MMP at ~55 kD; *, nonspecific bands; #, degradation forms (K). Bar graphs represent mean ± SE. *, $P < 0.05$; **, $P < 0.01$; ***, $P < 0.001$; determined by Student's t test.
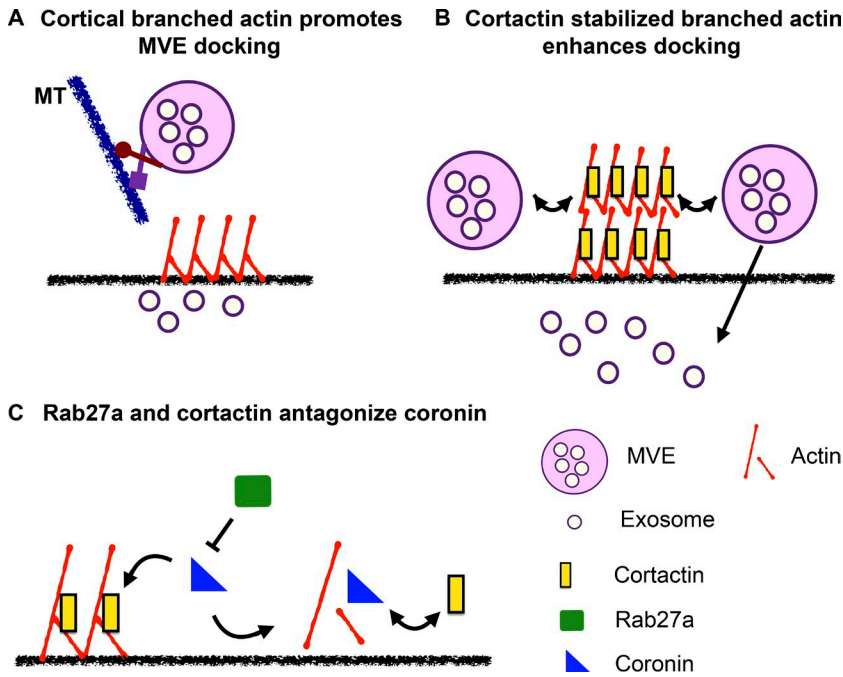
A Cortical branched actin promotes MVE docking

B Cortactin stabilized branched actin enhances docking

C Rab27a and cortactin antagonize coronin

MVE

Exosome

Cortactin

Rab27a

Coronin

Actin

Figure 9. **Model for regulation of exosome secretion by cortactin, Rab27a, and coronin.** (A) Cortical branched actin helps create MVE docking sites, such as invadopodia (Hoshino et al., 2013b) at the PM. (B) Cortactin stabilizes branched actin (Weaver et al., 2001), which enhances MVE docking. (C) Coronin antagonizes cortactin at actin branch points (Cai et al., 2008), leading to destabilization of actin branches and fewer MVE docking sites. Rab27a opposes this antagonism by inhibiting coronin binding to invadopodia-associated actin (Fig. 6, C–E), potentially by sequestration (Kimura et al., 2010; Yokoyama et al., 2011).

Functionally, purified exosomes fully rescue cortactin-KD cell defects in serum-independent growth and Transwell invasion.

Exosome secretion occurs when MVEs fuse with the PM. An alternative fate for exosomes is degradation after MVE fusion with lysosomes. How the balance between secretion and degradation is regulated is unclear. We previously found that invadopodia are key docking sites for MVEs and that the number of invadopodia can control the number of exosomes secreted from cells (Hoshino et al., 2013b). In this new study, we investigated the role of cortactin, which regulates branched actin assembly on both late endosomes (Hong et al., 2015) and at invadopodial MVE docking sites (Hoshino et al., 2013b). Our studies with KD cells indicate that cortactin controls both the number of moving MVEs and the number of PM docking sites, whereas overexpression of cortactin only affects MVE docking. The trafficking data (Fig. S3) together with our previous studies (Sung et al., 2011; Kirkbride et al., 2012; Hong et al., 2015) suggest that cortactin plays an essential role in LE maturation, such that cortactin loss leads to LE/Lys dysfunction and decreased numbers of MVEs that can be trafficked to the PM. Because cortactin-overexpressed cells did not affect MVE trafficking and only regulated MVE docking, we focused on that phenotype for further in-depth studies. We found that control of branched actin assembly is critical to create MVE docking sites.

Numerous membrane trafficking pathways are controlled by Rab GTPases (Stenmark, 2009). Among them, Rab27a is a critical MVE docking factor (Ostrowski et al., 2010). Rab27a also regulates peripheral capture and docking of other LE/Lys organelles, such as melanosomes and T cell granules (Hume et al., 2001; Marks and Seabra, 2001; Wu et al., 2001; Jordens et al., 2006; Ménasché et al., 2008). As Rabs function through multiple effectors, it is likely that the process of exosome secretion requires multiple events. For example, the synaptotagmin-like proteins Slp4 and Slp2a control exosome secretion from HeLa cells and T cell granule exocytosis (Ménasché et al., 2008; Ostrowski et al., 2010) and likely link Rab27a-bound organelles to the PM. Likewise, Rab27a binding to MyoVa allows off-loading of LE/Lys organelles from microtubules to peripheral actin

assemblies (Hume et al., 2001; Marks and Seabra, 2001; Wu et al., 2001; Jordens et al., 2006). Our data indicate that Rab27a has an additional function in docking, which is to regulate actin dynamics at cortical docking sites by preventing coronin 1b localization (Fig. 9). This might occur by the GDP-form of Rab27a sequestering coronin (Kimura et al., 2010), whereas the GTP form promotes tethering via SLPs (Ostrowski et al., 2010).

The role of cortical actin in vesicle docking and fusion is not well understood (Eitzen, 2003; Cingolani and Goda, 2008). On one hand, cortical actin must be disassembled for vesicles to access and bind the PM (Porat-Shliom et al., 2013). On the other hand, actin meshworks are known to promote vesicle docking (Eitzen, 2003). Cortical actin docking sites may capture vesicles by connecting to other cytoskeletal elements, including unconventional myosins carrying vesicles or by linking to microtubules, which are major vesicle transport highways. They may also act as signaling platforms that facilitate vesicle docking and fusion by creating specialized lipid domains (Fratti et al., 2004; Regazzi, 2007; Gabel et al., 2015). Invadopodia have all of these features: dynamic actin assembly, microtubule capture, and concentration of phosphoinositides, lipid raft components, and other signaling molecules (Murphy and Courtneidge, 2011; Hoshino et al., 2013a). At this point, the full mechanism of how dynamic invadopodial actin promotes MVE docking is not clear; however, our data indicate that actin stabilization is a key regulatory point.

Structure–function analysis of cortactin revealed that binding to the Arp2/3 complex and actin filaments is critical for control of exosome secretion. These data are consistent with our finding that molecules that regulate actin stability also control exosome secretion. Surprisingly, neither the Src phosphorylation sites nor the SH3 binding domain of cortactin were necessary for exosome secretion. Although these moieties could be considered regulatory sites, Src phosphorylation of cortactin has been shown to regulate actin dynamics in breast cancer cell invadopodia through binding of cofilin and Nck1 (Oser et al., 2009, 2010; Kirkbride et al., 2011). In addition, the SH3 domain of cortactin binds key invadopodia regulators N-WASp

and dynamin (Kirkbride et al., 2011), and we previously found that inhibition of N-WASp reduces both invadopodia formation and exosome secretion (Hoshino et al., 2013b). As N-WASp and dynamin have numerous protein and phospholipid binding partners (Takenawa and Suetsugu, 2007; Ferguson and De Camilli, 2012), we speculate that cortactin is not essential in our cells to recruit them to invadopodia; however, it is likely that these cortactin-binding interactions are key in many cells, depending on the signaling and cytoskeletal state.

Cortactin is known to regulate aggressive cancer cell traits, including tumor growth, cancer cell invasion and motility, and serum- and anchorage-independent growth (Kirkbride et al., 2011). The mechanisms by which cortactin controls many of these functions are unclear but could involve in situ control of cytoskeletal motility structures, secretion, or signaling (Kirkbride et al., 2011). Our finding that cortactin-KD cell defects in serum-independent growth and Transwell invasion can be rescued by incubation with physiological levels of purified exosomes suggests that regulation of exosome secretion may be a key mechanism by which cortactin promotes tumor aggressiveness. Thus, exosomes could contribute growth and angiogenic factors to promote tumor cell survival and in vivo growth as well as proteinases or extracellular matrix molecules to promote cellular invasiveness (Hoshino et al., 2013b; Wendler et al., 2013; Sung et al., 2015; Young et al., 2015). Our MT1-MMP-KD experiments suggest that MT1-MMP is not an essential exosome cargo for invasion through Matrigel, but that does not rule out activities of other proteinases. Indeed, multiple cargoes may act synergistically to promote exosome-induced phenotypes. An important future direction will be to fully explore the contribution of exosome secretion and specific exosome cargoes to the promotion of tumor aggressiveness by cortactin.

In summary, cortactin promotes exosome secretion from cancer cells by regulating branched actin stability. Our data suggest that modulation of branched actin dynamics is a critical control point for MVE docking and exosome secretion.

Materials and methods

Antibodies
Antibodies used were mouse anti-TSG101 (clone 4a10; GeneTex), mouse anti-Flotillin1 (610820; BD), mouse anticortactin (4F11; EMD Millipore), rabbit anti-CD63 for WB (ab68418 or ab134045; Abcam) and mouse anti-CD63 for immunofluorescence or endocytosis-EM studies (ab8219; Abcam), mouse anti–coronin 1b for WB (ab119071; Abcam), rabbit anti–coronin 1b for IF (gift from J.E. Bear, University of North Carolina Chapel Hill, Chapel Hill, NC), rabbit anti-EGFR (1005: sc-03; Santa Cruz Biotechnology, Inc.), rabbit anti-MMP9 (ab38898; Abcam), rabbit anti-Rab27 for WB (r4655; Sigma-Aldrich), mouse anti-MMP2 (F68; Daiichi Fine Chemical), rabbit collagen type 1 (600-406-103; Rockland), and mouse anti-MT1-MMP (clone ID8; Mori et al., 2002).

Cell lines and constructs
SCC61 cells were maintained in DMEM with 20% FBS with 0.4 µg/ml hydrocortisone. HT1080 and MDA-MB-231 cells were maintained in DMEM with 10% FBS. For live imaging experiments, cells were switched to L15 media and imaged at 37°C. EGFP-CD63 was a gift from G. Griffiths (Cambridge Institute for Medical Research, Cambridge, England, UK). Stable knockdown or stable expression of genes was achieved using the ViraPower Lentiviral expression

system (Thermo Fisher Scientific) according to the manufacturer's protocol. Expression of polyclonal stable cell lines was checked by WB, and cells were passaged for no longer than a month before discarding and thawing early-passage cultures. mEGFP-F-Tractin was a gift of R. Fischer (National Heart, Lung, and Blood Institute, Bethesda, MD) and was created by cloning the 9–52 stretch of the F-actin–binding protein ITPKA (Johnson and Schell, 2009) into pCMV-Tag2A-mGFP (Agilent Technologies). For mCherry-MMP9, pCEP4-MMP9 (Miyamori et al., 2001) was used as a PCR template for MMP9, which was then subcloned into pENTR vector (Thermo Fisher Scientific) and recombined into pLenti6-v5/mCherry destination vector (Nagano et al., 2010) using Gateway cloning (Thermo Fisher Scientific). EGFP-Rab5 Q79L construct was from Addgene. shRNA (Rab27a-1: 5′-GTGCGATCA AATGGTCATGCC-3′) and shLacZ were cloned into pLenti6/Block iT (Thermo Fisher Scientific) as previously described (Hoshino et al., 2013b), lentiviral shRNA constructs for coronin 1b were from Dharmacon (KD1: TRCNC0000116423 and KD2: TRCNC0000116424), MT1-MMPs were also from Dharmacon (sh1: TRCN0000050853 and sh3: TRCN0000050855); cortactin-KD1 (5′-GCACGAGTCACAGAG AGAT-3′) and cortactin-KD2 (5′-AAGCTGAGGGAGAATGTCT-3′ or scrambled 5′-GACCGCACATGAGATGAGA-3′) shRNAs inserted into pRetroSuper (originally from Reuven Agami) were previously described (Clark et al., 2007). Stable cortactin expression constructs were made by cloning full-length or mutant mouse cortactin molecules from pCDNA (Weed et al., 2000) or LZRS constructs (Sung et al., 2011) into pEntr/D-TOPO (Thermo Fisher Scientific) and then recombined into pLenti6-v5 (Thermo Fisher Scientific) by Gateway cloning (Thermo Fisher Scientific).

Isolation of exosomes from conditioned medium
SCC61 and HT1080 cells were cultured to 80% confluence for 48 h in Opti-MEM (except for Fig. 5 D, which was for 24 h, or for Fig. 7 I, which used DMEM for 48 h). Conditioned media was subjected to serial centrifugation to respectively sediment live cells (300 g for 10 min), dead cells (2,000 g [4,000 rpm in Ti45 rotor] for 30 min), microvesicles (10,000 g for 30 min [9,300 rpm in Ti45]), and UC exosomes (100,000 g [30,000 rpm in Ti45] for 18 h or 70 min). For further purification of UC exosomes by density gradient, a discontinuous iodixanol gradient was prepared. Solutions (40% wt/vol, 20% wt/vol, 10% wt/vol, and 5% wt/vol) of iodixanol were made by diluting OptiPrep (60% wt/vol aqueous iodixanol; Axis-Shield PoC) with 0.25 M sucrose/10 mM Tris, pH 7.5, from the bottom to the top of a 14 × 89–mm polyallomer tube. UC exosomes were added on top of the gradient and a continuous gradient was made through UC at 100,000 g (24,000 rpm in SW40 Ti rotor) for 18 h. 12 DG fractions were collected and diluted in PBS before pelleting through another round of ultracentrifugation at 100,000 g for 3 h, followed by washing and resuspension in PBS. All extracellular vesicle preparations were counted by nanoparticle tracking analysis (Nanosight LM10; Malvern, Ltd.).

Immunofluorescence
To visualize CD63 in Rab5Q79L-positive endosomes, $5 × 10^5$ SCC61 control and cortactin-KD cells were cultured on FN-coated glass coverslips in six-well or 35-mm dishes. Cells were transfected with EGFP-Rab5Q79L and 24 h later were fixed using 4% paraformaldehyde for 10 min and then permeabilized for 15 min with 0.1% Saponin in 3% BSA in PBS. Primary antibody anti-CD63 (Abcam) was incubated in 0.05% Saponin (A18820; Alfa Aeser) and 3% BSA (RPI) in PBS for 1 h at room temperature. Secondary antibody anti–mouse Alexa Fluor 633, and rhodamine phalloidin in 3% BSA in PBS were incubated for 1 h at room temperature. Cells were mounted in Aquapolymount (Polysciences, Inc.) and imaged at room temperature. Similar steps were followed for immunofluorescent staining of CD63 in other experiments.

Light microscopy

Confocal images were obtained with an LSM 510 (63× Plan-Apochromat objective; fixed imaging; ZEISS) or LSM 710 (63× Plan-Apochromat objective; ZEISS) using Argon2, HeNe, and HeNe2 lasers (live imaging) and Zen software (ZEISS). TIRF images were obtained with a TiE inverted light microscope (Nikon) equipped with a perfect focus, TIRF illuminator (Nikon), a 100×/1.49 NA TIRF objective (used in combination with a 1.5× optivar), Neo 5.5 cMOS camera (Andro), Sapphire 488- and 561-nm 50-mW lasers (Coherent, Inc.), and Elements software (Nikon).

Imaging conditions and data analysis

For confocal live-cell imaging, cells were transiently transfected with EGFP-CD63. After 24 h, images were captured every 2 s for 2 min. Imaris image processing software (Bitplane) was used to track CD63-positive MVEs from the confocal images to determine mean squared displacement of each MVE. A defined area located away from the nuclear region of each cell was selected for analysis (see representative tracks within the areas in Fig. S3 B). Endosomes >2 µm in size were excluded from the analysis. The autoregressive model algorithm was used and the tracks were generated. Diffusion coefficients (D; given as micrometers squared) were calculated from the tracks.

For TIRF live-cell imaging, cells were plated on dishes coated with 25 µg/ml fibronectin. After 24 h, images were captured every 100 ms for 30 s. For the shallow TIRF movies, imaging was performed with a standard laser angle to observe only fluorescence present at the cell–substrate interface, whereas for the deeper TIRF movies, the depth of penetration was calculated to be up to 1 µm from the PM using fluorescent 5-µµ bead standards (FS05F; Bangs Laboratories). For TIRF imaging of fixed immunostained cells, images were captured with a standard laser angle to observe CD63 puncta present at the cell–substrate interface. Secondary antibodies for cortactin and CD63 were tagged with Alexa Fluor 546 and 488, respectively. For visualizing actin turnover at invadopodia, cells transiently transfected with eGFP-F-Tractin were treated with 10 µM latrunculin A (L5163; Sigma-Aldrich) and TIRF images were captured every 20 ms for 2 min.

TIRF image analysis. For all TIRF analyses of MVEs, the center of the cell was excluded by drawing a circle, such as that as shown in Fig. 4 A. The remaining area, which is ~15–20 µm from the cell periphery, was used for the analysis. For quantification of docked MVEs in TIRF fixed-cell experiments, automated thresholding in Speckle Tracker plugin in Fiji was used to identify MVEs. Thresholding was based only on intensity not on vesicle size. MVE number and cell area data were exported to Excel for calculation of MVE number/area. For shallow TIRF movies, the levels for all movies were all reduced to the same level to lower nonspecific background. Then automated thresholding in Speckle Tracker plugin in Fiji was used to identify MVEs. Mobile MVEs were defined as MVE that had a change in x, y coordinates. Immobile MVEs defined in the graph were those that were immobile for ≥5 s. In deeper TIRF movies, MVEs were manually selected using Speckle Tracker plugin feature. The data generated was further processed using Count Speckle Displacement plugin in Fiji to determine the number of MVEs as well as calculate diffusion coefficients. For analysis of actin turnover in invadopodia from TIRF movies, ImageJ plugin Intensity versus time monitor was used to determine actin fluorescence intensity at invadopodia for 4 × 4–pixel areas. A separate 4 × 4–pixel area outside of each invadopodia was selected to determine the background fluorescence intensity. The specific invadopodia actin fluorescence intensity was determined by subtracting the neighboring cytoplasmic background intensity from the total invadopodia actin fluorescence intensity. The data were then normalized to the frame at which Latrunculin A was added. GraphPad Prism version 6 was used to plot the data and nonlinear regression analysis was used to determine the half-life of actin fluorescence intensity decay.

Serum-independent growth assay

On day 1, 25,000 cells were seeded in six-well dishes in medium containing serum. The next day, cells were washed three times with PBS. Serum-free media with or without the addition of exosomes was then added. After 4 d, cells were trypsinized and counted using a hemocytometer.

Transwell invasion assay

25,000 cells were seeded on the top of BD Biocoat Matrigel-coated invasion chambers (8.0-µm pore size for 24-well plates) in the presence of 2.5% exosome-depleted serum in DMEM on both sides of the filter. When added, exosomes derived from control or KD cells were added together with the cells on the topside of the filter. 48 h later, cells were removed from the top of the filter using cotton swabs before staining for cells that had migrated to the bottom of the filter (Hematology staining kit; Richard Allen Scientific). Five bright-field images per insert were taken using an Eclipse TE2000-E microscope (Nikon) equipped with a 20× Plan-Fluor 0.3 NA objective. Cells per image were counted and averaged per replicate.

Invadopodia assay

50,000 cells were seeded on 35-mm MatTek dishes coated with 10 µM FITC-FN/2% cross-linked gelatin, prepared as previously described (Clark and Weaver, 2008). Cells were cultured in invadopodia media (1:1 ratio of DMEM and RPMI media containing 10% FBS [HyClone], 5% Nuserum [Gibco], and 20 ng/ml EGF [Invitrogen]) for 18 h before fixing and immunostaining. Cells were fixed with 4% PFA for 10 min, permeabilized using 0.1% Triton X-100 in 3% BSA for 10 min, blocked with 3% BSA for 20 min. Cells were then incubated overnight with anti-coronin 1b (1:250) at 4°C. The next day, cells were incubated with Rhodamine-Phalloidin (1:2,000) and secondary Alexa Fluor 633 (1:500) for 1 h at room temperature. Invadopodia plates were then mounted in antifade mounting reagent before imaging. Functional invadopodia, indicated by dark holes in the fluorescent matrix (FITC-FN) colocalized with actin puncta, were analyzed for absolute intensity of coronin 1b or actin within a boxed area of 4 × 4 pixels surrounding the actin puncta. A similar procedure was done for cortactin immunostaining, except that the cells were plated on Alexa Fluor 633/FN and the secondary antibody for cortactin was conjugated to Alexa Fluor 488.

EM

For negative staining of purified exosomes, Formvar carbon film–coated grids (FCF-200-Cu; Electron Microscopy Sciences) were washed in double distilled water, followed by 100% ethanol. For each step, excess liquid was removed by wicking with filter paper. 10-µl samples were added to grids for 5 min. Grids were immediately stained with 2% phosphotungstic acid, pH 6.1, for 20s and allowed to dry overnight. Grids were imaged using a FEI Tecnai T12 TEM (120 kV LaB6 source), Gatan cryotransfer stage, and AMT XR41-S side-mounted 2K × 2K CCD camera, 2102 SC. All exosome images were collected at 50,000× with an Advanced Microscopy Techniques CCD camera.

TEM of whole unlabeled cells was performed as previously described (Kirkbride et al., 2012). For visualization of CD63-positive MVEs, SCC61 control and cortactin-KD1 cells were incubated for 30 min at 37°C with anti-CD63 antibody (ab8219; Abcam) labeled with HRP (Z 25054; Molecular Probes). Cells were then washed with PBS and fixed for 1 h in 3% glutaraldehyde in 0.1 M sodium cacodylate (NaCaC) buffer. After several washes in 0.1 M NaCaC, cells were incubated with DAB (EMS Chemical) in 0.05 M Tris-HCl at pH 7.6. The

enzymatic reaction was started by adding H_2O_2 to a final concentration of 0.01% and allowed to proceed for 30 min. The cells were washed three times with 0.05 M Tris-HCl buffer. After a brief wash with water, cells were washed three times with 0.1 M NaCaC buffer. The cells were then postfixed with 1% osmium tetroxide in 0.1 M NaCaC buffer, then washed with 0.1 M NaCaC buffer. Next, cells were scraped and pelleted, resuspended in 0.1 M NaCaC buffer, and washed with water. The cells were then incubated with 1% uranyl acetate (en bloc) for 10 min. Next, cells were dehydrated through a graded ethanol series (30%, 50%, 75%, 85%, and 95%) for 15 min each. Cells were further dehydrated with 100% ethanol and propylene oxide (PO). After this, cells were infiltrated with a 3:1 mixture of PO and epoxy resin for 30 min then 1:1 ratio of PO and resin for 1 h and subsequently overnight. The next day, samples were infiltrated with 1:3 mixture of PO and resin followed by six changes of pure resin for 36 h. Then the pellet was embedded for 48 h in epoxy resin at 60°C. Sections (70 nm) were collected on copper grids and cells were counterstained with 2% uranyl acetate and Reynold's lead citrate. Samples were imaged on FEI/Tecnai 12 electron microscope at various magnifications.

Mass spectrometry and liquid chromatography MS/MS analysis

Shotgun proteomic analysis of purified exosomes was performed by first resuspending the exosomes in LDS sample buffer (Thermo Fisher Scientific), resolving the proteins ~1 cm using a 10% Novex precast gel, and then performing in-gel tryptic digestion to recover peptides. The peptides were analyzed via MudPIT (Multidimensional Protein Identification Technology) essentially as described earlier (MacCoss et al., 2002; Martinez et al., 2012). In brief, digested peptides were loaded onto a biphasic precolumn consisting of 4 cm of reversed-phase (RP) material followed by 4 cm of strong cation-exchange material. Once loaded, the column was placed in line with a 20-cm RP analytical column packed into a nanospray emitter tip directly coupled to a linear ion trap mass spectrometer (LTQ). A subset of peptides was eluted from the strong cation-exchange material onto the RP analytical via a pulse of volatile salt, separated by an RP gradient and then ionized directly into the mass spectrometer where both the intact masses (mass spectrometry [MS]) and fragmentation patters (MS/MS) of the peptides were collected. The peptide spectral data were used to query a protein database using Sequest (Yates et al., 1995) and the resulting identifications were collated and filtered using IDPicker (Ma et al., 2009) and Scaffold (http://www.proteomesoftware.com). Relative protein abundances and statistical significance of differences were evaluated via spectral counting techniques using the Quasitel program (Li et al., 2010). Quasitel uses a quasi-Poisson likelihood model to obtain multiple testing corrected p-value calculations, based on both spectral count consistency across biological replicates and the magnitude of the differences between experimental and control groups (Li et al., 2010). Protein groups were classified using UniProt database and a Venn diagram was made using Microsoft Excel for Mac 2011, version 14.4.8.

Data analysis and statistics

For both quantitated data and representative images from experiments, the *n* value and independent experiment numbers are listed in the figure legends. For nonquantitated WBs (e.g., checking knockdown or overexpression), they were generally performed a single time. All statistical analysis was performed using SPSS version 22, and graphs were generated in Prism GraphPad version 5 or 6. All data were first tested for normality using a Kolmogorov–Smirnov normality test. Parametric data were analyzed by a two-tailed *t* test and plotted with bar graphs showing mean ± standard error (SE) or scatterplots showing the mean. Data that were nonparametric were analyzed by Mann–Whitney *U* test and plotted using box and whiskers plots, where the median is shown as a line, the box indicates 25–75th percentile, and the whiskers indicate 5–95th percentile or scatterplots showing the median.

Online supplemental material

Table S1 is an Excel spreadsheet with Quasitel, gene ontology, and coefficient of variation analyses of exosome cargo proteomics data. Fig. S1 shows a characterization of cortactin expression levels and additional extracellular vesicle data from SCC61, HT1080, and MDA-MB-231 cells. Fig. S2 shows electron microscopic images of CD63-labeled MVEs in control and cortactin-KD cells. Fig. S3 shows analysis of MVE number and speed from confocal movies of GFP-CD63 in control, cortactin-KD, and cortactin-overexpressed cells. Fig. S4 shows an analysis of MVE docking from TIRF fixed images and movies, with representative images and diffusion constant analysis. Fig. S5 shows images and analysis of invadopodial actin intensity in cortactin-KD cells along with images and analysis of invadopodial cortactin and actin intensity and matrix degradation in coronin 1b–KD cells. Video 1 shows confocal imaging of MVE trafficking in Sc, cortactin-overexpressed, and cortactin-KD cells. Video 2 shows TIRF imaging (shallow angle) of MVE docking in Sc control cells. Video 3 shows TIRF imaging (shallow angle) of MVE docking in in KD cells. Video 4 shows TIRF imaging (shallow angle) of MVE docking in cortactin-overexpressed cells. Video 5 shows TIRF imaging (shallow angle) of MVE docking in Rab27a-KD1 cells. Video 6 shows TIRF imaging (deeper angle, illumination up to 1 µm into the cell) of MVE docking in Sc control cells. Video 7 shows TIRF imaging (deeper angle, illumination up to 1 µm into the cell) of MVE docking in cortactin-KD1 cells. Video 8 shows TIRF imaging (deeper angle, illumination up to 1 µm into the cell) of MVE docking in cortactin-OE cells. Video 9 shows TIRF imaging (deeper angle, illumination up to 1 µm into the cell) of MVE docking in Rab27a-KD1 cells. Video 10 shows actin turnover at invadopodia in shLacZ control cells, Rab27a-KD, cortactin-overexpressed, and cortactin-overexpressed Rab27a-KD cells. Online supplemental material is available at http://www.jcb.org/cgi/content/full/jcb.201601025/DC1.

References

Aatonen, M.T., T. Ohman, T.A. Nyman, S. Laitinen, M. Grönholm, and P.R. Siljander. 2014. Isolation and characterization of platelet-derived extracellular vesicles. *J. Extracell. Vesicles.* 3. http://dx.doi.org/10.3402/jev.v3.24692

Aharon, A., T. Tamari, and B. Brenner. 2008. Monocyte-derived microparticles and exosomes induce procoagulant and apoptotic effects on endothelial cells. *Thromb. Haemost.* 100:878–885.

Allaire, P.D., M. Seyed Sadr, M. Chaineau, E. Seyed Sadr, S. Konefal, M. Fotouhi, D. Maret, B. Ritter, R.F. Del Maestro, and P.S. McPherson. 2013. Interplay between Rab35 and Arf6 controls cargo recycling to coordinate cell adhesion and migration. *J. Cell Sci.* 126:722–731. http://dx.doi.org/10.1242/jcs.112375

Baietti, M.F., Z. Zhang, E. Mortier, A. Melchior, G. Degeest, A. Geeraerts, Y. Ivarsson, F. Depoortere, C. Coomans, E. Vermeiren, et al. 2012. Syndecan-syntenin-ALIX regulates the biogenesis of exosomes. *Nat. Cell Biol.* 14:677–685. http://dx.doi.org/10.1038/ncb2502

Bobrie, A., S. Krumeich, F. Reyal, C. Recchi, L.F. Moita, M.C. Seabra, M. Ostrowski, and C. Théry. 2012. Rab27a supports exosome-dependent and -independent mechanisms that modify the tumor microenvironment and can promote tumor progression. *Cancer Res.* 72:4920–4930. http://dx.doi.org/10.1158/0008-5472.CAN-12-0925

Cai, L., A.M. Makhov, D.A. Schafer, and J.E. Bear. 2008. Coronin 1B antagonizes cortactin and remodels Arp2/3-containing actin branches in lamellipodia. *Cell.* 134:828–842. http://dx.doi.org/10.1016/j.cell.2008.06.054

Choudhuri, K., J. Llodrá, E.W. Roth, J. Tsai, S. Gordo, K.W. Wucherpfennig, L.C. Kam, D.L. Stokes, and M.L. Dustin. 2014. Polarized release of T-cell-receptor-enriched microvesicles at the immunological synapse. *Nature.* 507:118–123. http://dx.doi.org/10.1038/nature12951

Cingolani, L.A., and Y. Goda. 2008. Actin in action: the interplay between the actin cytoskeleton and synaptic efficacy. *Nat. Rev. Neurosci.* 9:344–356. http://dx.doi.org/10.1038/nrn2373

Clark, E.S., and A.M. Weaver. 2008. A new role for cortactin in invadopodia: regulation of protease secretion. *Eur. J. Cell Biol.* 87:581–590. http://dx.doi.org/10.1016/j.ejcb.2008.01.008

Clark, E.S., A.S. Whigham, W.G. Yarbrough, and A.M. Weaver. 2007. Cortactin is an essential regulator of matrix metalloproteinase secretion and extracellular matrix degradation in invadopodia. *Cancer Res.* 67:4227–4235. http://dx.doi.org/10.1158/0008-5472.CAN-06-3928

Clark, E.S., B. Brown, A.S. Whigham, A. Kochaishvili, W.G. Yarbrough, and A.M. Weaver. 2009. Aggressiveness of HNSCC tumors depends on expression levels of cortactin, a gene in the 11q13 amplicon. *Oncogene.* 28:431–444. http://dx.doi.org/10.1038/onc.2008.389

Corrigan, L., S. Redhai, A. Leiblich, S.J. Fan, S.M. Perera, R. Patel, C. Gandy, S.M. Wainwright, J.F. Morris, F. Hamdy, et al. 2014. BMP-regulated exosomes from Drosophila male reproductive glands reprogram female behavior. *J. Cell Biol.* 206:671–688. http://dx.doi.org/10.1083/jcb.201401072

Costa-Silva, B., N.M. Aiello, A.J. Ocean, S. Singh, H. Zhang, B.K. Thakur, A. Becker, A. Hoshino, M.T. Mark, H. Molina, et al. 2015. Pancreatic cancer exosomes initiate pre-metastatic niche formation in the liver. *Nat. Cell Biol.* 17:816–826. http://dx.doi.org/10.1038/ncb3169

Desnos, C., J.S. Schonn, S. Huet, V.S. Tran, A. El-Amraoui, G. Raposo, I. Fanget, C. Chapuis, G. Ménasché, G. de Saint Basile, et al. 2003. Rab27A and its effector MyRIP link secretory granules to F-actin and control their motion towards release sites. *J. Cell Biol.* 163:559–570. http://dx.doi.org/10.1083/jcb.200302157

Dong, W.W., Q. Mou, J. Chen, J.T. Cui, W.M. Li, and W.H. Xiao. 2012. Differential expression of Rab27A/B correlates with clinical outcome in hepatocellular carcinoma. *World J. Gastroenterol.* 18:1806–1813. http://dx.doi.org/10.3748/wjg.v18.i15.1806

Eitzen, G. 2003. Actin remodeling to facilitate membrane fusion. *Biochim. Biophys. Acta.* 1641:175–181. http://dx.doi.org/10.1016/S0167-4889(03)00087-9

EL Andaloussi, S., I. Mäger, X.O. Breakefield, and M.J. Wood. 2013. Extracellular vesicles: biology and emerging therapeutic opportunities. *Nat. Rev. Drug Discov.* 12:347–357. http://dx.doi.org/10.1038/nrd3978

Ferguson, S.M., and P. De Camilli. 2012. Dynamin, a membrane-remodelling GTPase. *Nat. Rev. Mol. Cell Biol.* 13:75–88.

Fratti, R.A., Y. Jun, A.J. Merz, N. Margolis, and W. Wickner. 2004. Interdependent assembly of specific regulatory lipids and membrane fusion proteins into the vertex ring domain of docked vacuoles. *J. Cell Biol.* 167:1087–1098. http://dx.doi.org/10.1083/jcb.200409068

Gabel, M., F. Delavoie, V. Demais, C. Royer, Y. Bailly, N. Vitale, M.F. Bader, and S. Chasserot-Golaz. 2015. Annexin A2-dependent actin bundling promotes secretory granule docking to the plasma membrane and exocytosis. *J. Cell Biol.* 210:785–800. http://dx.doi.org/10.1083/jcb.201412030

Ghossoub, R., F. Lembo, A. Rubio, C.B. Gaillard, J. Bouchet, N. Vitale, J. Slavík, M. Machala, and P. Zimmermann. 2014. Syntenin-ALIX exosome biogenesis and budding into multivesicular bodies are controlled by ARF6 and PLD2. *Nat. Commun.* 5:3477. http://dx.doi.org/10.1038/ncomms4477

Greening, D.W., R. Xu, H. Ji, B.J. Tauro, and R.J. Simpson. 2015. A protocol for exosome isolation and characterization: evaluation of ultracentrifugation, density-gradient separation, and immunoaffinity capture methods. *Methods Mol. Biol.* 1295:179–209. http://dx.doi.org/10.1007/978-1-4939-2550-6_15

Hendrix, A., D. Maynard, P. Pauwels, G. Braems, H. Denys, R. Van den Broecke, J. Lambert, S. Van Belle, V. Cocquyt, C. Gespach, et al. 2010. Effect of the secretory small GTPase Rab27B on breast cancer growth, invasion, and metastasis. *J. Natl. Cancer Inst.* 102:866–880. http://dx.doi.org/10.1093/jnci/djq153

Ho, J.R., E. Chapeaublanc, L. Kirkwood, R. Nicolle, S. Benhamou, T. Lebret, Y. Allory, J. Southgate, F. Radvanyi, and B. Goud. 2012. Deregulation of Rab and Rab effector genes in bladder cancer. *PLoS One.* 7:e39469. http://dx.doi.org/10.1371/journal.pone.0039469

Hong, N.H., A. Qi, and A.M. Weaver. 2015. PI(3,5)P2 controls endosomal branched actin dynamics by regulating cortactin-actin interactions. *J. Cell Biol.* 210:753–769. http://dx.doi.org/10.1083/jcb.201412127

Hoshino, A., B. Costa-Silva, T.L. Shen, G. Rodrigues, A. Hashimoto, M. Tesic Mark, H. Molina, S. Kohsaka, A. Di Giannatale, S. Ceder, et al. 2015. Tumour exosome integrins determine organotropic metastasis. *Nature.* 527:329–335. http://dx.doi.org/10.1038/nature15756

Hoshino, D., K.M. Branch, and A.M. Weaver. 2013a. Signaling inputs to invadopodia and podosomes. *J. Cell Sci.* 126:2979–2989. http://dx.doi.org/10.1242/jcs.079475

Hoshino, D., K.C. Kirkbride, K. Costello, E.S. Clark, S. Sinha, N. Grega-Larson, M.J. Tyska, and A.M. Weaver. 2013b. Exosome secretion is enhanced by invadopodia and drives invasive behavior. *Cell Reports.* 5:1159–1168. http://dx.doi.org/10.1016/j.celrep.2013.10.050

Hsu, C., Y. Morohashi, S. Yoshimura, N. Manrique-Hoyos, S. Jung, M.A. Lauterbach, M. Bakhti, M. Grønborg, W. Möbius, J. Rhee, et al. 2010. Regulation of exosome secretion by Rab35 and its GTPase-activating proteins TBC1D10A-C. *J. Cell Biol.* 189:223–232. http://dx.doi.org/10.1083/jcb.200911018

Huang, C., J. Liu, C.C. Haudenschild, and X. Zhan. 1998. The role of tyrosine phosphorylation of cortactin in the locomotion of endothelial cells. *J. Biol. Chem.* 273:25770–25776. http://dx.doi.org/10.1074/jbc.273.40.25770

Hume, A.N., L.M. Collinson, A. Rapak, A.Q. Gomes, C.R. Hopkins, and M.C. Seabra. 2001. Rab27a regulates the peripheral distribution of melanosomes in melanocytes. *J. Cell Biol.* 152:795–808. http://dx.doi.org/10.1083/jcb.152.4.795

Hyenne, V., A. Apaydin, D. Rodriguez, C. Spiegelhalter, S. Hoff-Yoessle, M. Diem, S. Tak, O. Lefebvre, Y. Schwab, J.G. Goetz, and M. Labouesse. 2015. RAL-1 controls multivesicular body biogenesis and exosome secretion. *J. Cell Biol.* 211:27–37. http://dx.doi.org/10.1083/jcb.201504136

Johnson, H.W., and M.J. Schell. 2009. Neuronal IP3 3-kinase is an F-actin-bundling protein: role in dendritic targeting and regulation of spine morphology. *Mol. Biol. Cell.* 20:5166–5180. http://dx.doi.org/10.1091/mbc.E09-01-0083

Jordens, I., W. Westbroek, M. Marsman, N. Rocha, M. Mommaas, M. Huizing, J. Lambert, J.M. Naeyaert, and J. Neefjes. 2006. Rab7 and Rab27a control two motor protein activities involved in melanosomal transport. *Pigment Cell Res.* 19:412–423. http://dx.doi.org/10.1111/j.1600-0749.2006.00329.x

Kimura, T., S. Taniguchi, and I. Niki. 2010. Actin assembly controlled by GDP-Rab27a is essential for endocytosis of the insulin secretory membrane. *Arch. Biochem. Biophys.* 496:33–37. http://dx.doi.org/10.1016/j.abb.2010.01.017

Kinley, A.W., S.A. Weed, A.M. Weaver, A.V. Karginov, E. Bissonette, J.A. Cooper, and J.T. Parsons. 2003. Cortactin interacts with WIP in regulating Arp2/3 activation and membrane protrusion. *Curr. Biol.* 13:384–393. http://dx.doi.org/10.1016/S0960-9822(03)00107-6

Kirkbride, K.C., B.H. Sung, S. Sinha, and A.M. Weaver. 2011. Cortactin: a multifunctional regulator of cellular invasiveness. *Cell Adhes. Migr.* 5:187–198. http://dx.doi.org/10.4161/cam.5.2.14773

Kirkbride, K.C., N.H. Hong, C.L. French, E.S. Clark, W.G. Jerome, and A.M. Weaver. 2012. Regulation of late endosomal/lysosomal maturation and trafficking by cortactin affects Golgi morphology. *Cytoskeleton (Hoboken).* 69:625–643. http://dx.doi.org/10.1002/cm.21051

Kucharzewska, P., H.C. Christianson, J.E. Welch, K.J. Svensson, E. Fredlund, M. Ringnér, M. Mörgelin, E. Bourseau-Guilmain, J. Bengzon, and M. Belting. 2013. Exosomes reflect the hypoxic status of glioma cells and mediate hypoxia-dependent activation of vascular cells during tumor

development. *Proc. Natl. Acad. Sci. USA.* 110:7312–7317. http://dx.doi.org/10.1073/pnas.1220998110

Lee, J.K., S.R. Park, B.K. Jung, Y.K. Jeon, Y.S. Lee, M.K. Kim, Y.G. Kim, J.Y. Jang, and C.W. Kim. 2013. Exosomes derived from mesenchymal stem cells suppress angiogenesis by down-regulating VEGF expression in breast cancer cells. *PLoS One.* 8:e84256. http://dx.doi.org/10.1371/journal.pone.0084256

Li, M., W. Gray, H. Zhang, C.H. Chung, D. Billheimer, W.G. Yarbrough, D.C. Liebler, Y. Shyr, and R.J. Slebos. 2010. Comparative shotgun proteomics using spectral count data and quasi-likelihood modeling. *J. Proteome Res.* 9:4295–4305. http://dx.doi.org/10.1021/pr100527g

Ma, Z.Q., S. Dasari, M.C. Chambers, M.D. Litton, S.M. Sobecki, L.J. Zimmerman, P.J. Halvey, B. Schilling, P.M. Drake, B.W. Gibson, and D.L. Tabb. 2009. IDPicker 2.0: Improved protein assembly with high discrimination peptide identification filtering. *J. Proteome Res.* 8:3872–3881. http://dx.doi.org/10.1021/pr900360j

MacCoss, M.J., W.H. McDonald, A. Saraf, R. Sadygov, J.M. Clark, J.J. Tasto, K.L. Gould, D. Wolters, M. Washburn, A. Weiss, et al. 2002. Shotgun identification of protein modifications from protein complexes and lens tissue. *Proc. Natl. Acad. Sci. USA.* 99:7900–7905. http://dx.doi.org/10.1073/pnas.122231399

Marks, M.S., and M.C. Seabra. 2001. The melanosome: membrane dynamics in black and white. *Nat. Rev. Mol. Cell Biol.* 2:738–748. http://dx.doi.org/10.1038/35096009

Martinez, M.N., C.H. Emfinger, M. Overton, S. Hill, T.S. Ramaswamy, D.A. Cappel, K. Wu, S. Fazio, W.H. McDonald, D.L. Hachey, et al. 2012. Obesity and altered glucose metabolism impact HDL composition in CETP transgenic mice: a role for ovarian hormones. *J. Lipid Res.* 53:379–389. http://dx.doi.org/10.1194/jlr.M019752

Martinez-Quiles, N., H.Y. Ho, M.W. Kirschner, N. Ramesh, and R.S. Geha. 2004. Erk/Src phosphorylation of cortactin acts as a switch on-switch off mechanism that controls its ability to activate N-WASP. *Mol. Cell. Biol.* 24:5269–5280. http://dx.doi.org/10.1128/MCB.24.12.5269-5280.2004

Ménasché, G., M.M. Ménager, J.M. Lefebvre, E. Deutsch, R. Athman, N. Lambert, N. Mahlaoui, M. Court, J. Garin, A. Fischer, and G. de Saint Basile. 2008. A newly identified isoform of Slp2a associates with Rab27a in cytotoxic T cells and participates to cytotoxic granule secretion. *Blood.* 112:5052–5062. http://dx.doi.org/10.1182/blood-2008-02-141069

Mittelbrunn, M., C. Gutiérrez-Vázquez, C. Villarroya-Beltri, S. González, F. Sánchez-Cabo, M.A. González, A. Bernad, and F. Sánchez-Madrid. 2011. Unidirectional transfer of microRNA-loaded exosomes from T cells to antigen-presenting cells. *Nat. Commun.* 2:282. http://dx.doi.org/10.1038/ncomms1285

Miyamori, H., T. Takino, Y. Kobayashi, H. Tokai, Y. Itoh, M. Seiki, and H. Sato. 2001. Claudin promotes activation of pro-matrix metalloproteinase-2 mediated by membrane-type matrix metalloproteinases. *J. Biol. Chem.* 276:28204–28211. http://dx.doi.org/10.1074/jbc.M103083200

Mori, H., T. Tomari, N. Koshikawa, M. Kajita, Y. Itoh, H. Sato, H. Tojo, I. Yana, and M. Seiki. 2002. CD44 directs membrane-type 1 matrix metalloproteinase to lamellipodia by associating with its hemopexin-like domain. *EMBO J.* 21:3949–3959. http://dx.doi.org/10.1093/emboj/cdf411

Morton, W.M., K.R. Ayscough, and P.J. McLaughlin. 2000. Latrunculin alters the actin-monomer subunit interface to prevent polymerization. *Nat. Cell Biol.* 2:376–378. http://dx.doi.org/10.1038/35014075

Murphy, D.A., and S.A. Courtneidge. 2011. The 'ins' and 'outs' of podosomes and invadopodia: characteristics, formation and function. *Nat. Rev. Mol. Cell Biol.* 12:413–426. http://dx.doi.org/10.1038/nrm3141

Nagano, M., D. Hoshino, T. Sakamoto, N. Kawasaki, N. Koshikawa, and M. Seiki. 2010. ZF21 protein regulates cell adhesion and motility. *J. Biol. Chem.* 285:21013–21022. http://dx.doi.org/10.1074/jbc.M110.106443

Oser, M., H. Yamaguchi, C.C. Mader, J.J. Bravo-Cordero, M. Arias, X. Chen, V. Desmarais, J. van Rheenen, A.J. Koleske, and J. Condeelis. 2009. Cortactin regulates cofilin and N-WASp activities to control the stages of invadopodium assembly and maturation. *J. Cell Biol.* 186:571–587. http://dx.doi.org/10.1083/jcb.200812176

Oser, M., C.C. Mader, H. Gil-Henn, M. Magalhaes, J.J. Bravo-Cordero, A.J. Koleske, and J. Condeelis. 2010. Specific tyrosine phosphorylation sites on cortactin regulate Nck1-dependent actin polymerization in invadopodia. *J. Cell Sci.* 123:3662–3673. http://dx.doi.org/10.1242/jcs.068163

Ostrowski, M., N.B. Carmo, S. Krumeich, I. Fanget, G. Raposo, A. Savina, C.F. Moita, K. Schauer, A.N. Hume, R.P. Freitas, et al. 2010. Rab27a and Rab27b control different steps of the exosome secretion pathway. *Nat. Cell Biol.* 12:19–30: 1–13. http://dx.doi.org/10.1038/ncb2000

Peinado, H., M. Alečković, S. Lavotshkin, I. Matei, B. Costa-Silva, G. Moreno-Bueno, M. Hergueta-Redondo, C. Williams, G. García-Santos, C. Ghajar, et al. 2012. Melanoma exosomes educate bone marrow progenitor cells toward a pro-metastatic phenotype through MET. *Nat. Med.* 18:883–891. http://dx.doi.org/10.1038/nm.2753

Porat-Shliom, N., O. Milberg, A. Masedunskas, and R. Weigert. 2013. Multiple roles for the actin cytoskeleton during regulated exocytosis. *Cell. Mol. Life Sci.* 70:2099–2121. http://dx.doi.org/10.1007/s00018-012-1156-5

Raposo, G., and W. Stoorvogel. 2013. Extracellular vesicles: exosomes, microvesicles, and friends. *J. Cell Biol.* 200:373–383. http://dx.doi.org/10.1083/jcb.201211138

Regazzi, R. 2007. Molecular Mechanisms of Exocytosis. Landes Bioscience/Eurekah.com;Springer Science+Business Media, New York. 178 pp.

Rodrigo, J.P., L.A. García, S. Ramos, P.S. Lazo, and C. Suárez. 2000. EMS1 gene amplification correlates with poor prognosis in squamous cell carcinomas of the head and neck. *Clin. Cancer Res.* 6:3177–3182.

Rodrigo, J.P., D. García-Carracedo, L.A. García, S. Menéndez, E. Allonca, M.V. González, M.F. Fresno, C. Suárez, and J.M. García-Pedrero. 2009. Distinctive clinicopathological associations of amplification of the cortactin gene at 11q13 in head and neck squamous cell carcinomas. *J. Pathol.* 217:516–523. http://dx.doi.org/10.1002/path.2462

Schuuring, E. 1995. The involvement of the chromosome 11q13 region in human malignancies: cyclin D1 and EMS1 are two new candidate oncogenes--a review. *Gene.* 159:83–96. http://dx.doi.org/10.1016/0378-1119(94)00562-7

Schuuring, E., E. Verhoeven, W.J. Mooi, and R.J. Michalides. 1992. Identification and cloning of two overexpressed genes, U21B31/PRAD1 and EMS1, within the amplified chromosome 11q13 region in human carcinomas. *Oncogene.* 7:355–361.

Singh, R.K., K. Mizuno, C. Wasmeier, S.T. Wavre-Shapton, C. Recchi, S.D. Catz, C. Futter, T. Tolmachova, A.N. Hume, and M.C. Seabra. 2013. Distinct and opposing roles for Rab27a/Mlph/MyoVa and Rab27b/Munc13-4 in mast cell secretion. *FEBS J.* 280:892–903.

Sorkin, A., and M. von Zastrow. 2009. Endocytosis and signalling: intertwining molecular networks. *Nat. Rev. Mol. Cell Biol.* 10:609–622. http://dx.doi.org/10.1038/nrm2748

Stenmark, H. 2009. Rab GTPases as coordinators of vesicle traffic. *Nat. Rev. Mol. Cell Biol.* 10:513–525. http://dx.doi.org/10.1038/nrm2728

Stenmark, H., R.G. Parton, O. Steele-Mortimer, A. Lütcke, J. Gruenberg, and M. Zerial. 1994. Inhibition of rab5 GTPase activity stimulates membrane fusion in endocytosis. *EMBO J.* 13:1287–1296.

Sung, B.H., X. Zhu, I. Kaverina, and A.M. Weaver. 2011. Cortactin controls cell motility and lamellipodial dynamics by regulating ECM secretion. *Curr. Biol.* 21:1460–1469. http://dx.doi.org/10.1016/j.cub.2011.06.065

Sung, B.H., T. Ketova, D. Hoshino, A. Zijlstra, and A.M. Weaver. 2015. Directional cell movement through tissues is controlled by exosome secretion. *Nat. Commun.* 6:7164. http://dx.doi.org/10.1038/ncomms8164

Takenawa, T., and S. Suetsugu. 2007. The WASP-WAVE protein network: connecting the membrane to the cytoskeleton. *Nat. Rev. Mol. Cell Biol.* 8:37–48. http://dx.doi.org/10.1038/nrm2069

Thery, C., S. Amigorena, G. Raposo, and A. Clayton. 2006. Isolation and characterization of exosomes from cell culture supernatants and biological fluids. *Curr. Protoc. Cell Biol.* Chapter 3:Unit 3.22. http://dx.doi.org/10.1002/0471143030.cb0322s30

Théry, C. 2011. Exosomes: secreted vesicles and intercellular communications. *F1000 Biol. Rep.* 3:15. http://dx.doi.org/10.3410/B3-15

Timpson, P., D.K. Lynch, D. Schramek, F. Walker, and R.J. Daly. 2005. Cortactin overexpression inhibits ligand-induced down-regulation of the epidermal growth factor receptor. *Cancer Res.* 65:3273–3280.

Timpson, P., A.S. Wilson, G.M. Lehrbach, R.L. Sutherland, E.A. Musgrove, and R.J. Daly. 2007. Aberrant expression of cortactin in head and neck squamous cell carcinoma cells is associated with enhanced cell proliferation and resistance to the epidermal growth factor receptor inhibitor gefitinib. *Cancer Res.* 67:9304–9314. http://dx.doi.org/10.1158/0008-5472.CAN-07-0798

Trajkovic, K., C. Hsu, S. Chiantia, L. Rajendran, D. Wenzel, F. Wieland, P. Schwille, B. Brügger, and M. Simons. 2008. Ceramide triggers budding of exosome vesicles into multivesicular endosomes. *Science.* 319:1244–1247. http://dx.doi.org/10.1126/science.1153124

van Balkom, B.W., O.G. de Jong, M. Smits, J. Brummelman, K. den Ouden, P.M. de Bree, M.A. van Eijndhoven, D.M. Pegtel, W. Stoorvogel, T. Würdinger, and M.C. Verhaar. 2013. Endothelial cells require miR-214 to secrete exosomes that suppress senescence and induce angiogenesis in human and mouse endothelial cells. *Blood.* 121:3997–4006: S1–S15. http://dx.doi.org/10.1182/blood-2013-02-478925

Weaver, A.M. 2008. Invadopodia. *Curr. Biol.* 18:R362–R364. http://dx.doi.org/10.1016/j.cub.2008.02.028

Weaver, A.M., A.V. Karginov, A.W. Kinley, S.A. Weed, Y. Li, J.T. Parsons, and J.A. Cooper. 2001. Cortactin promotes and stabilizes Arp2/3-induced actin filament network formation. *Curr. Biol.* 11:370–374. http://dx.doi.org/10.1016/S0960-9822(01)00098-7

Weed, S.A., A.V. Karginov, D.A. Schafer, A.M. Weaver, A.W. Kinley, J.A. Cooper, and J.T. Parsons. 2000. Cortactin localization to sites of actin assembly in lamellipodia requires interactions with F-actin and the Arp2/3 complex. *J. Cell Biol.* 151:29–40. http://dx.doi.org/10.1083/jcb.151.1.29

Wendler, F., N. Bota-Rabassedas, and X. Franch-Marro. 2013. Cancer becomes wasteful: emerging roles of exosomes(†) in cell-fate determination. *J. Extracell. Vesicles.* 2. http://dx.doi.org/10.3402/jev.v2i0.22390

Wu, X., K. Rao, M.B. Bowers, N.G. Copeland, N.A. Jenkins, and J.A. Hammer III. 2001. Rab27a enables myosin Va-dependent melanosome capture by recruiting the myosin to the organelle. *J. Cell Sci.* 114:1091–1100.

Yáñez-Mó, M., P.R. Siljander, Z. Andreu, A.B. Zavec, F.E. Borràs, E.I. Buzas, K. Buzas, E. Casal, F. Cappello, J. Carvalho, et al. 2015. Biological properties of extracellular vesicles and their physiological functions. *J. Extracell. Vesicles.* 4:27066. http://dx.doi.org/10.3402/jev.v4.27066

Yates, J.R. III, J.K. Eng, A.L. McCormack, and D. Schieltz. 1995. Method to correlate tandem mass spectra of modified peptides to amino acid sequences in the protein database. *Anal. Chem.* 67:1426–1436. http://dx.doi.org/10.1021/ac00104a020

Yokoyama, K., H. Kaji, J. He, C. Tanaka, R. Hazama, T. Kamigaki, Y. Ku, K. Tohyama, and Y. Tohyama. 2011. Rab7a negatively regulates phagocytosis by prolongation of the actin-coating stage around phagosomes. *J. Biol. Chem.* 286:5375–5382. http://dx.doi.org/10.1074/jbc.M110.171702

Young, C.D., L.J. Zimmerman, D. Hoshino, L. Formisano, A.B. Hanker, M.L. Gatza, M.M. Morrison, P.D. Moore, C.A. Whitwell, B. Dave, et al. 2015. Activating PIK3CA mutations induce an epidermal growth factor receptor (EGFR)/extracellular signal-regulated kinase (ERK) paracrine signaling axis in basal-like breast cancer. *Mol. Cell. Proteomics.* 14:1959–1976. http://dx.doi.org/10.1074/mcp.M115.049783

Yuan, B.Z., X. Zhou, D.B. Zimonjic, M.E. Durkin, and N.C. Popescu. 2003. Amplification and overexpression of the EMS 1 oncogene, a possible prognostic marker, in human hepatocellular carcinoma. *J. Mol. Diagn.* 5:48–53. http://dx.doi.org/10.1016/S1525-1578(10)60451-5